A disrupted compartment boundary underlies abnormal cardiac patterning and congenital heart defects

Irfan S. Kathiriya[1,#], Martin H. Dominguez[2,3,4], Kavitha S. Rao[1,2], Jonathon M. Muncie-Vasic[2], W. Patrick Devine[2,5], Kevin M. Hu[1,2,6], Swetansu K. Hota[2,7], Bayardo I. Garay[1,8], Diego Quintero[2,9], Piyush Goyal[1,2,10], Megan N. Matthews[1], Reuben Thomas[2], Tatyana Sukonnik[2,15], Dario Miguel-Perez[2], Sarah Winchester[2], Emily F. Brower[2], André Forjaz[11], Pei-Hsun Wu[11], Denis Wirtz[11], Ashley L. Kiemen[11], Benoit G. Bruneau[2,12,13,14,#]

[#]corresponding authors

[1] Department of Anesthesia and Perioperative Care, University of California, San Francisco, San Francisco, CA

[2] Gladstone Institutes, San Francisco, CA

[3] Department of Medicine, University of California, San Francisco, San Francisco, CA

[4] Current address: Department of Medicine (Cardiovascular Medicine), Perelman School of Medicine, University of Pennsylvania, Philadelphia, PA

[5] Current address: Department of Pathology, University of California, San Francisco, San Francisco, CA

[6] Current address: Creighton University School of Medicine, Omaha, NE

[7] Current address: Herman B. Wells Center for Pediatric Research, Indiana University School of Medicine, Indianapolis, IN

[8] Current address: University of Minnesota Medical Scientist Training Program, Minneapolis, MN

[9] Current address: Department of Human Genetics, Emory University School of Medicine, Atlanta, GA

[10] Current address: Touro University California, Vallejo, CA

[11] Department of Chemical and Biomolecular Engineering, Johns Hopkins University, Baltimore, MD

[12] Roddenberry Center for Stem Cell Biology and Medicine, Gladstone Institutes, San Francisco, CA

[13] Cardiovascular Research Institute, University of California, San Francisco, San Francisco, CA

[14] Department of Pediatrics, University of California, San Francisco, San Francisco, CA

[15] Deceased

Abstract.

Failure of septation of the interventricular septum (IVS) is the most common congenital heart defect (CHD), but mechanisms for patterning the IVS are largely unknown. We show that a *Tbx5*$^{+}$/*Mef2cAHF*$^{+}$ progenitor lineage forms a compartment boundary bisecting the IVS. This coordinated population originates at a first- and second heart field interface, subsequently forming a morphogenetic nexus. Ablation of *Tbx5*$^{+}$/*Mef2cAHF*$^{+}$ progenitors cause IVS disorganization, right ventricular hypoplasia and mixing of IVS lineages. Reduced dosage of the CHD transcription factor TBX5 disrupts boundary position and integrity, resulting in ventricular septation defects (VSDs) and patterning defects, including *Slit2* and *Ntn1* misexpression. Reducing NTN1 dosage partly rescues cardiac defects in *Tbx5* mutant embryos. Loss of *Slit2* or *Ntn1* causes VSDs and perturbed septal lineage distributions. Thus, we identify essential cues that direct progenitors to pattern a compartment boundary for proper cardiac septation, revealing new mechanisms for cardiac birth defects.

Main.

Organogenesis relies on fine tissue patterning, and disturbances cause organ malformations that result in birth defects. Examples of prevalent birth defects resulting from

abnormal patterning include congenital limb abnormalities, neural tube defects or congenital heart defects (CHDs).

CHDs are the most common birth defects and are a leading cause of morbidity and mortality in childhood. CHDs are thought to result from alterations to the orchestrated patterning of heart development. Nearly half of patients with CHDs have ventricular septal defects (VSDs) or atrial septal defects (ASDs), either in isolation or combined with other anatomic defects, including abnormal chamber formation. For example, atrioventricular canal (AVC) defects include VSDs, ASDs and abnormal development of the atrioventricular (AV) valves, with severe cases leading to chamber hypoplasia and functional single ventricle physiology. There is a large gap in our understanding of how early developmental events pattern cardiac morphogenesis and anatomy. Addressing this understudied need can inform diagnostic prognosis, family planning and therapeutic approaches for CHDs.

Complete atrioventricular septation into four chambers allows for separation of systemic and pulmonary circulations and enables higher levels of oxygen for transport in arterial blood. Indeed, some progress has been made to determine the embryonic origins of the IVS [1,23]. A dye-labelled approach in chick embryos revealed that labelling of the ventral surface of the linear heart tube becomes positioned at the outer curvature of the linear heart tube [1,2]. When labelled at the outer curvature upon rightward looping, the label was found at the apical border of the primary interventricular foramen [1,2]. Discovery of the *Ganglion Nodosum* epitope from chick, which demarcated the primary interventricular foramen and subsequently the IVS, AV junction and ventricular conduction system in mouse, chick and humans, led to the description of a “primary ring” for the ventricular septum [3–5].

Discrete early cardiac progenitors in mesoderm contribute to specific cardiac anatomy [6–8]. The first heart field (FHF) gives rise primarily to the left ventricle (LV) and parts of the atria, while the second heart field (SHF) contributes predominantly to the right ventricle (RV), outflow tract (OFT) and portions of the atria [9]. The heart fields can be largely recapitulated by marking

77 lineage-labelled progenitors at gastrulation. Specifically, a lineage labelled by the CHD-linked
78 transcription factor *Tbx5* (*Tbx5*$^+$-lineage) contributes to the LV and atria, while the anterior heart
79 field enhancer of *Mef2c* (*Mef2cAHF*$^+$)-lineage largely contributes to the RV and OFT [6].

80 An aspect of proper tissue patterning entails the establishment of compartment
81 boundaries to separate neighboring fields of cells that exhibit discrete functions [10–12]. Few
82 compartment boundaries have been identified in mammals, including in the limb [13–15] and at the
83 midbrain-hindbrain border [16]. In the developing heart, both the LV and RV lineages supply
84 descendants to the interventricular septum (IVS) and establish a mutual border between the two
85 lineages [6,17]. Clonal analysis shows segregation at the IVS of the two lineages into non-
86 intermingling cellular compartments, on either the left or right sides of the IVS [6,17]. This lineage
87 configuration is reminiscent of a compartment boundary[10–12]. Using an intersectional-lineage
88 labelling approach, a subset of cardiac progenitor cells labeled by both *Tbx5*$^+$*/Mef2cAHF*$^+$ were
89 described with contributions to the left side of this apparent compartment boundary [6].
90 Understanding the role of the *Tbx5*$^+$*/Mef2cAHF*$^+$ lineage-labeled compartment boundary at the
91 IVS may reveal clues about IVS patterning with potential relevance for VSD etiologies. More
92 broadly, how disturbances to compartment boundaries contribute to birth defects is largely
93 unknown.

94 Here, we combined genetic lineage labeling with light sheet microscopy to follow
95 contributions of *Tbx5*$^+$*/Mef2cAHF*$^+$ precursors to a compartment boundary during cardiac
96 morphogenesis. We ablated *Tbx5*$^+$*/Mef2cAHF*$^+$ precursors to determine the essential roles of the
97 lineage-labeled compartment boundary for cardiac septation and chamber development. By
98 leveraging a genetic lesion of the CHD gene *Tbx5,* our work uncovers the genetic regulation of
99 the *Tbx5*$^+$*/Mef2cAHF*$^+$ lineage-labeled compartment boundary for proper IVS patterning. We
100 deployed single cell RNA sequencing (scRNAseq) to discover novel Tbx5-sensitive cues that are
101 essential for compartment boundary regulation and formation of the IVS during heart
102 development.

103

104 Results.

105 Early cardiac progenitors for the IVS, IAS and AVC. We used conditional dual lineage labelling
106 by *Tbx5*$^{CreERT2/+}$ or *Mef2cAHF-DreERT2* and marked cells during gastrulation at embryonic day
107 (E)6.5 by tamoxifen-induced recombination. We followed reporter-labeled lineages by
108 epifluorescence microscopy, histology or light sheet microscopy (Figure 1). At E14.5, the *Tbx5*$^{+}$
109 lineage contributed to the left side of the IVS, often ending at a presumptive line marked at the
110 apex by the interventricular (IV) groove, consistent with previous reports suggesting a lineage
111 boundary [6,17]. *Tbx5*$^{+}$ and *Mef2cAHF*$^{+}$ lineages showed largely complementary patterns, with
112 notable overlap of *Tbx5*$^{+}$ and *Mef2cAHF*$^{+}$ lineages at the IVS, AVC and IAS (Figure 1B, D, F). To
113 better visualize the *Tbx5*$^{+}$*/Mef2cAHF*$^{+}$ lineage, we used a conditional intersectional-lineage
114 labeling approach. Using lineage reporters responsive to both CreERT2 and DreERT2 [18], we
115 observed a striking spatial pattern of the *Tbx5*$^{+}$*/Mef2cAHF*$^{+}$ lineage in the IVS, AVC and IAS. At
116 E14.5, the septal lineage extended to the apex of the heart via the IVS, to the base of the heart
117 at the AV canal, as well as to the IAS superiorly[15–18] (Figure 1H-J). These results expanded upon
118 previous findings in the developing IVS at E10.5 [6], by identifying contributions from
119 *Tbx5*$^{+}$*/Mef2cAHF*$^{+}$ progenitors to additional anatomic sites during chamber formation and
120 septation. Moreover, lineage contributions to sites of cardiac septation were derived from
121 *Tbx5*$^{+}$*/Mef2cAHF*$^{+}$ progenitors at E6.5 (Supp. Figure 1), but not later at E8.5 or E10.5, implicating
122 a narrow, early window for capturing *Tbx5*$^{+}$*/Mef2cAHF*$^{+}$ septal progenitors during cardiac
123 mesoderm formation.

124

125 *Tbx5*$^{+}$*/Mef2cAHF*$^{+}$ septal lineage is prefigured in early mouse heart development. To characterize
126 the lineage derived from *Tbx5*$^{+}$*/Mef2cAHF*$^{+}$-septal progenitors during early heart development, we
127 examined the localization of the lineage prior to heart tube formation at E8.0 (Figure 2, Video 1).
128 By light sheet imaging, the pattern of the *Tbx5*$^{+}$*/Mef2cAHF*$^{+}$ lineage was detected at the dorsal

129 aspect of the *Tbx5*$^{+}$ lineage, at an interface between the presumptive first and second heart fields
130 (Figure 2A-E"). Cell segmentation at this early stage revealed that the *Tbx5*$^{+}$*/Mef2cAHF*$^{+}$ lineage
131 resembled a nascent halo of cells that became readily apparent at later stages of heart
132 development (Figure 2F-I).

133 We further examined the lineage contributions of *Tbx5*$^{+}$*/Mef2cAHF*$^{+}$ septal progenitors at
134 subsequent timepoints during cardiac morphogenesis by light sheet microscopy. At the linear
135 heart tube stage at E8.25, the labeled *Tbx5*$^{+}$*/Mef2cAHF*$^{+}$ lineage appeared intricately arranged
136 into a ring of cells between the future left and right ventricles (Figure 2J, K). This circlet
137 configuration was maintained during rightward looping of the heart at E8.5 (Figure 2O-Q) and
138 subsequent chamber formation. At E10.5, we observed a band of lineage-labeled cells from the
139 IV groove at the outer curvature to the inner curvature near the AV groove that extended
140 posteriorly to the atria (Figure 2R-T), reminiscent of the "primary ring" [3–5]. Optical sections showed
141 the labeled lineage superiorly at a crossroads of the AVC, outflow tract and atria (Figure 2S). This
142 populates a morphogenetic nexus, where VSDs can occur due to abnormal connections between
143 the IVS and the AV cushions, outflow tract cushions, or the muscular septum itself. In the atria,
144 we noted lineage-labeled cells at the midline, superiorly and inferiorly, suggesting that the
145 Tbx5^{+}/Mef2cAHF^{+} lineage potentially marks the presumptive location of the IAS for later stages
146 (Supp. Figure 2B-E). Consequently, this data is consistent with a notion that the *Tbx5*$^{+}$*/Mef2cAHF*$^{+}$
147 lineage is configured early in heart development, well before subsequent morphogenetic events
148 of chamber formation and cardiac septation.

149

150 <u>IVS disorganization and ventricular hypoplasia from cell ablation of *Tbx5*$^{+}$/*Mef2cAHF*$^{+}$</u>
151 <u>progenitors</u>. To determine a role for the *Tbx5*$^{+}$*/Mef2cAHF*$^{+}$ septal progenitors during heart
152 development, we conditionally ablated these cells at E6.5. To this end, we generated an
153 intersectional recombinase-responsive *DTA176* knock-in mouse allele at the *Hip11* safe-harbor
154 locus, by which cells would be killed where approximately 100-200 molecules of DTA176 were

155 expressed [19]. Upon tamoxifen administration to pregnant dams at E6.5, intersectional-*DTA* mutant
156 (*Tbx5*$^{CreERT2/+}$*; Mef2cAHF-DreERT2; Hip11*$^{Intersectional\text{-}DTA176/+}$) embryos displayed RV hypoplasia at
157 E9.5 (Figure 3A, B) and E12.5 (Figure 3C-J), together with IVS disorganization and non-
158 compaction with a blunted IV groove (Figure 3H, J). Further, there were defects of the AV
159 cushions and absence of the IAS (Figure 3H, J). A few *Tbx5*$^{+}$*/Mef2cAHF*$^{+}$ lineage cells remained
160 in mutant embryos, likely reflecting some degree of inefficient dual recombination of both the
161 reporter allele and the intersectional-*DTA* transgene. Beyond E12.5, intersectional-*DTA* mutant
162 embryos were not recovered. Hence, these findings suggested that the *Tbx5*$^{+}$*/Mef2cAHF*$^{+}$ septal
163 progenitors were not only important for IVS development and AV septation, but also for RV
164 chamber formation.
165
166 <u>Lineage mixing from disruption of an IVS compartment boundary upon ablation of</u>
167 <u>*Tbx5*$^{+}$*/Mef2cAHF*$^{+}$ septal progenitors</u>. We hypothesized that the *Tbx5*$^{+}$*/Mef2cAHF*$^{+}$ septal
168 progenitors establish a compartment boundary at the IVS. Upon ablation of *Tbx5*$^{+}$*/Mef2cAHF*$^{+}$
169 septal progenitors, we predicted that if either lineage expanded into the other ventricular chamber,
170 then this would suggest lineage mixing from loss of compartment boundary integrity. To determine
171 if *Tbx5*$^{+}$*/Mef2cAHF*$^{+}$ septal progenitors were essential for a compartment boundary at the IVS, we
172 tested the effects of ablating *Tbx5*$^{+}$*/Mef2cAHF*$^{+}$ septal progenitors on lineage segregation. We
173 quantified the distributions of the *Mef2cAHF*$^{+}$ or *Tbx5*$^{+}$ lineages at E10.5 after tamoxifen
174 administration at E6.5, by quantifying fluorescence intensity as a linear profile across the
175 ventricular chambers by light sheet microscopy. In control (*Tbx5*$^{CreERT2/+}$*;Mef2cAHF-*
176 *DreERT2;Hip11*$^{+/+}$) (n=2) embryos at E10.5, cells of the *Mef2cAHF*$^{+}$ lineage were enriched in the
177 RV. Cells of the *Tbx5*$^{+}$ lineage were highly enriched in the LV and rarely found in the RV, and
178 both lineages overlapped at the developing IVS. This data was consistent with observations of
179 lineage segregation at the IVS during later stages of heart development. However, in mutant
180 intersectional-*DTA* (*Tbx5*$^{CreERT2/+}$*;Mef2cAHF-DreERT2;Hip11*$^{Intersectional\text{-}DTA176/+}$) (n=2) embryos at

181 E10.5, cells of the *Mef2cAHF*$^{+}$ lineage were less leftward in the corresponding region of targeted
182 cell ablation, suggesting a rightward retreat of the Mef2cAHF^{+} lineage from ablation of
183 *Tbx5*$^{+}$*/Mef2cAHF*$^{+}$ progenitors. In contrast, cells of the Tbx5^{+} lineage in intersectional-*DTA*
184 mutants were observed more rightward, including in the RV. Therefore, we inferred that
185 *Tbx5*$^{+}$*/Mef2cAHF*$^{+}$ progenitors were essential for preventing lineage mixing between the RV and
186 LV, by maintaining compartment boundary integrity at the developing IVS. This implies a
187 preferential regulation of first heart field derivatives over the adjacent second heart field.
188
189 Heterozygous loss of *Tbx5* in the IVS leads to VSDs. *TBX5* is a transcription factor gene that
190 causes VSDs in Holt-Oram Syndrome from haploinsufficiency in humans [20–22] and mice [23]. We
191 wondered if heterozygous loss of *Tbx5* in the IVS alone would cause VSDs. We used the
192 *Mef2cAHF-Cre* [24] in combination with a conditional deletion of *Tbx5* (*Tbx5*^{flox}) [23], to conditionally
193 delete *Tbx5* heterozygously in a domain that overlaps with *Tbx5* expression at the IVS [25]. We
194 observed membranous VSDs in *Mef2cAHF-Cre*;*ROSA26*$^{mTmG/+}$*;Tbx5*$^{flox/+}$ mutant embryos (n=4/7)
195 compared to controls (n=0/3), at E14.5 (Supp. Figure 3A-C). This result contrasted with a previous
196 report that did not identify VSDs, albeit using a mixed genetic background [26]. This provided
197 evidence that appropriate *Tbx5* dosage in the IVS was essential for proper ventricular septation.
198
199 Disturbed septal lineage contributions from reduced *Tbx5.* As TBX5 dosage reduction globally or
200 only in the IVS results in VSDs, we reasoned that reducing TBX5 dosage may affect the regulation
201 of the *Tbx5*$^{+}$*/Mef2cAHF*$^{+}$ septal progenitors and their subsequent lineage contributions. We
202 evaluated a reduction of *Tbx5* using a hypomorphic (*Tbx5*^{CreERT2}) allele [22] in combination with a
203 conditional deletion of *Tbx5* (*Tbx5*^{flox}) [23] at E6.5. This resulted in levels of *Tbx5* that are estimated
204 to be about 25% of wildtype in the *Tbx5*$^{+}$ lineage. In control (*Tbx5*$^{CreERT2/+}$*;Mef2cAHF-*
205 *DreERT2;ROSA26*$^{Ai66/Ai6}$) embryos, the *Tbx5*$^{+}$*/Mef2cAHF*$^{+}$ septal lineage overlapped at the
206 lineage front of the *Tbx5*$^{+}$ lineage in the IVS, from the base to the apex of the heart at the IV

207 groove, spanning from anterior to posterior of the heart in the IVS (Figure 4A-A", Supp. Figure
208 4A, B, Video 2). Among *Tbx5*$^{CreERT2/flox}$ mutant (*Tbx5*$^{CreERT2/flox}$*;Mef2cAHF-*
209 *DreERT2;ROSA26*$^{Ai66/Ai6}$) embryos, we found that reduced TBX5 dosage at E6.5 caused a
210 spectrum of defects, frequently including VSDs, ASDs and AVC defects at E14.5 (Figure 4B-D'),
211 reminiscent of features of Holt-Oram Syndrome [20,21,27]. The normally organized distribution of the
212 tdTomato$^+$ cells was highly irregular in the *Tbx5*$^{CreERT2/flox}$ mutant hearts regardless of VSDs (Supp.
213 Figure 4A-H). Often, tdTomato$^+$ cells were less apparent in the posterior IVS (Figure 4A', A", B',
214 B", C', C", D'), and tdTomato$^+$ cells were nearly absent in a heart that displayed a severe AVC
215 defect and chamber hypoplasia (Figure 4D, D', Supp Figure 4G, H).

216 We used quantitative morphometry to assess the position and distribution of the
217 *Tbx5*$^+$*/Mef2cAHF*$^+$ septal lineage at the IVS. We tested this by quantifying linear profiles of the
218 labeled *Tbx5*$^+$*/Mef2cAHF*$^+$ septal lineage in the heart. We found that both distribution and position
219 of the *Tbx5*$^+$*/Mef2cAHF*$^+$ septal lineage was disturbed in *Tbx5*$^{CreERT2/flox}$ mutant (n=3; control,
220 n=4)(Figure 4E-H, Supp. Figure 4I, J), including an increase of tdTomato$^+$ cells leftward in the LV,
221 suggesting abnormal lineage position. As well, we observed a broader band of *Tbx5*$^+$*/Mef2cAHF*$^+$
222 septal lineage cells, suggesting that proper TBX5 dosage maintains integrity of the compartment
223 boundary marked by the *Tbx5*$^+$*/Mef2cAHF*$^+$ lineage at the IVS (Figure 4G, H). We also observed
224 a reduction, or sometimes absence, of the labeled septal lineage among AVC cells, as well as
225 remnant atrial septal tissue in *Tbx5*$^{CreERT2/flox}$ mutants (Figure 4D, D').

226 We further observed that cells of the *Tbx5*$^+$*/Mef2cAHF*$^+$ lineage in the IVS were arranged
227 like a stack of coins, especially from the apex to the mid-septum (Figure 4A"). We wondered if
228 proper TBX5 dosage might be necessary for maintaining appropriate cell orientation in the IVS.
229 Therefore, cell alignment was determined and quantified by two metrics, average orientation
230 score or directional coherency. In *Tbx5*$^{CreERT2/flox}$ mutant hearts, *Tbx5*$^+$*/Mef2cAHF*$^+$ lineage
231 (tdTomato$^+$) and *Tbx5*$^+$ lineage (ZsGreen$^+$) cells were reduced in the dominant direction of cell
232 orientation and were more frequently in the orientation orthogonal to the dominant direction

233 (Figure 4S, Supp. Figure 4T). Further, both lineages demonstrated worse directional coherency
234 in *Tbx5*$^{CreERT2/flox}$ mutants (Figure 4T, Supp. Figure 4U), implicating TBX5 in proper cell orientation
235 in the IVS.
236
237 <u>*Tbx5*-sensitive genes encode guidance cues</u>. To find downstream effectors of Tbx5 that may
238 mediate the regulation of *Tbx5*$^{+}$*/Mef2cAHF*$^{+}$ lineage cells, we applied scRNAseq at E13.5, prior
239 to completion of ventricular septation. We micro-dissected the RV, LV and IVS+AVC in controls
240 and *Tbx5* mutants (*Tbx5*$^{CreERT2/flox}$*;Mef2cAHF-DreERT2;ROSA26*$^{Ai66/Ai6}$) (Figure 5A). These
241 samples were labeled at E6.5 for progenitors of the *Tbx5*$^{+}$*/Mef2cAHF*$^{+}$ lineage (*tdTomato*$^{+}$) and
242 *Tbx5*$^{+}$ lineage (*ZsGreen*$^{+}$). In samples from each cardiac tissue region, we detected clusters
243 enriched for *Tnnt2*$^{+}$ cardiomyocytes (CMs), *Postn*$^{+}$ fibroblasts, *Plvap*$^{+}$ endothelial cells,
244 *Tbx18*$^{+}$*/Wt1*$^{+}$ epicardial cells, *Hba-x*$^{+}$ red blood cells, and *C1qb*$^{+}$ white blood cells (Figure 5B,
245 Supp. Figure 5A-F).
246 In particular, *tdTomato*$^{+}$ cells were most abundant among clusters of *Tnnt2*$^{+}$
247 cardiomyocytes (CMs) of the IVS+AVC region (Figure 5C). However, we were unable to identify
248 a gene expression signature that was unique to the *Tbx5*$^{+}$/*Mef2cAHF*$^{+}$ lineage, beyond the lineage
249 marker itself, at this stage. Likewise, *ZsGreen*$^{+}$ cells were also enriched among clusters of *Tnnt2*$^{+}$
250 CMs in this region (Figure 5D), indicative of the *Tbx5*$^{+}$ lineage contribution to CMs in the region,
251 as well as a site of conditional reduction of *Tbx5* among *Tbx5* mutants.
252 We then focused our analysis on a subset of *Tnnt2*$^{+}$ enriched clusters from IVS+AV canal
253 regions. We identified genotype-enriched clusters that were abundant with cells from controls
254 (Cluster 5) or *Tbx5* mutants (Cluster 10) (Figure 5E, F). Control-enriched cluster 5 included genes
255 expressed in the AV canal region, encoding the Wnt co-receptor *Rspo3*, morphogen *Bmp2*, and
256 transcription factors *Tbx2* and *Tbx3*, suggesting that these genes are reduced in *Tbx5* mutants
257 (Figure 5G, H). As well, the SLIT-receptor *Robo1,* which is implicated in mouse and human VSDs
258 [28–30], and Netrin-receptor *Unc5b,* were also downregulated in *Tbx5* mutant cells (Figure 5G, H).

259 In the mutant-enriched cluster 10, genes typically expressed in ventricular trabeculae were
260 enriched (Figure 5G, H). These included natriuretic peptide *Nppa*, transcription factor *Cited1,* and
261 bone morphogenetic protein *Bmp10*, suggesting ectopic expression of these trabecular genes in
262 the IVS of *Tbx5* mutants. Intriguingly, guidance cues *Netrin1* (*Ntn1)* and *Slit2,* which are best
263 known for axonal development or vasculogenesis [31], were also dysregulated (Figure 5G, H).
264 We examined differential gene expression between controls or *Tbx5* mutants in *tdTomato*$^+$
265 (Tbx5$^+$/Mef2cAHF$^+$ septal lineage) or *ZsGreen*$^+$ (Tbx5$^+$ lineage) CMs. We found many
266 differentially expressed genes that overlapped among comparisons of *tdTomato*$^+$ or *ZsGreen*$^+$
267 clusters, including *Nppa*, *Cited1,* and *Slit2*, consistent with findings from cluster-to-cluster
268 comparisons (Supp. Figure 5G, H).
269 We used orthogonal assays to validate candidate TBX5-sensitive genes. By fluorescence
270 *in situ* hybridization in formalin fixed paraffin embedded (FFPE) sections, we observed a reduction
271 of gene expression of *Bmp2, Robo1 and Unc5b* in the AV canal region of mutant hearts when
272 compared to controls. (Supp. Figure S6M-X'). As well, we detected expansion of *Nppa* and *Slit2*
273 into the IVS and compact layer of mutant hearts, both of which are normally expressed only in the
274 trabecular regions of both ventricles of control hearts (Figure 5I-L'). Moreover, we discovered
275 *Ntn1* expression enriched in LV trabeculae and in a gradient across the control IVS (Figure 5M,
276 M'), consistent with immunostaining of NTN1 in the heart at E14.5 (Supp. Figure 6Y). Notably,
277 *Ntn1* was enriched in the LV earlier at E11.5 during ventricular septation (Supp. Figure 6Z).
278 However, in *Tbx5* mutants, the *Ntn1* gradient was flattened and expanded in the IVS by reduced
279 Tbx5 dosage (Figure 5N, N'). Interestingly, we observed abnormal *Nppa*, *Slit2* and *Ntn1* in *Tbx5*
280 mutants with or without VSDs, suggesting that this dysregulated gene expression was not
281 secondary to VSDs (Supp Figure 6A-L'). In addition, analysis of ChIP-seq of TBX5 from
282 embryonic mouse hearts [32] showed TBX5 occupancy at promoters of *Nppa, Slit2*, and *Ntn1* (Supp
283 Figure 7A-C), suggesting these guidance genes are likely to be direct targets of TBX5 in the heart.
284

285 *Tbx5-Slit2* and *Tbx5-Ntn1* genetic interactions. We evaluated if genetic interactions existed
286 between *Tbx5* and *Slit2* or *Ntn1*. As *Tbx5* heterozygous mutant (*Tbx5*$^{del/+}$) [23] mouse embryos
287 display muscular or membranous VSDs, we wondered if heterozygous *Slit2* or *Ntn1* loss of
288 function (LOF) mutant embryos might alter *Tbx5*-dependent phenotypes. We mated *Tbx5*$^{del/+}$ mice
289 with either *Slit2* (*Slit2*$^{+/-}$) or *Ntn1* (*Ntn1*$^{beta\text{-}actin\text{-}Cre/+}$ referred here subsequently as *Ntn1*$^{+/-}$ [33,34])
290 heterozygous LOF mice. In *Tbx5*$^{del/+}$ embryos at E14.5, we observed membranous (n=5/8) or
291 muscular (n=3/8) VSDs by histology (Supp. Figure 8B, E), consistent with previous reports [23].
292 Among *Slit2*$^{+/-}$ embryos at E14.5, we observed a membranous VSD (n=1/8) (Supp. Figure 8C, E).
293 This contrasted with a previous report that did not detect any VSDs in *Slit2*$^{+/-}$ albeit using a
294 different mutant *Slit2* allele [28]. In *Tbx5*$^{del/+}$;*Slit2*$^{+/-}$ compound heterozygous embryos, we observed
295 an estimated decrease in the incidence of membranous VSDs (n=5/8) (Supp. Figure 8D, E), which
296 approached significance (log OR -2.5; $p<0.09$ in a Generalized Linear Model).

297 We next tested if there was a genetic interaction between *Tbx5* and *Ntn1* (Supp. Figure
298 8F-J). In *Ntn1*$^{+/-}$embryos, we observed a membranous (n=1/9) or a muscular (n=1/9) VSD. In
299 *Tbx5*$^{del/+}$;*Ntn1*$^{+/-}$ compound heterozygous embryos, we observed a significant decrease of
300 membranous VSDs (n=1/8; log OR -5.3; $p<1x10^{-3}$ by a Generalized Linear Model), but not
301 significant changes to prevalence of muscular VSDs (n=4/8; log OR 0.12; $p<0.93$), consistent with
302 a genetic interaction between *Tbx5* and *Ntn1* for ventricular septation.

303 We wondered if there were other quantitative histologic differences, in addition to the
304 changes in incidence of VSD types. To quantify morphometry from histology, we leveraged a
305 deep learning algorithm, known a CODA [35], to detect embryonic mouse heart components from
306 hematoxylin and eosin (H&E) sections. We generated three-dimensional (3-D) tissue
307 reconstructions, to visualize and quantify anatomic structures and CHDs, including membranous
308 and muscular VSDs, at cellular resolution (Figure 6I-K). Using this machine learning method, we
309 discovered that the cell density of the IVS, which we termed IVS fill, was increased in *Tbx5*$^{del/+}$;
310 *Ntn1*$^{+/-}$ embryos compared to wildtype ($p<0.05$ by Fisher's exact test), while classification of the

311 IVS as trabecular was significantly reduced in *Tbx5*$^{del/+}$;*Ntn1*$^{+/-}$ embryos ($p<0.05$ by Fisher's exact
312 test) (Supp. Figure 8M). In addition, we estimated the minimal area for each membranous or
313 muscular VSD, when present (Supp. Figure 8O, P). In *Tbx5*$^{del/+}$;*Slit2*$^{+/-}$ compound mutants, we
314 detected statistically significant levocardia ($p<0.001$ by Fisher's exact test), as determined by the
315 axis of the heart compared to the spine and sternum (Supp. Figure 8Q). This uncovered a genetic
316 interaction between *Tbx5* and *Slit2* related to heart position, demonstrating that machine learning-
317 based morphometry can quantify unexpected anatomic findings.
318
319 <u>*Slit2* and *Ntn1* for ventricular septation.</u> To determine if *Slit2* or *Ntn1* are essential for ventricular
320 septation, we evaluated homozygous LOF mouse mutants for *Slit2* or *Ntn1* for VSDs. In *Slit2*$^{-/-}$
321 embryos at E14.5, we observed that homozygous loss of *Slit2* displayed complete penetrance for
322 VSDs, including membranous (n=4/4; log OR 5.0, $p<0.00$) or muscular VSD (n=1/4) (Figure 6A-
323 D), demonstrating a far higher incidence than a previous report using an alternative *Slit2* LOF
324 allele [28]. Further, we detected a statistically significant non-compacted IVS as determined by
325 reduced IVS fill and thinning of the right ventricular compact layer (Supp. Figure 9E, H). Likewise,
326 *Ntn1*$^{-/-}$ embryos displayed membranous VSDs (n=6/7), an apparent thinning of the ventricular
327 compact layer and a non-compacted IVS, although these observations were not statistically
328 significant (Supp. Figure 9). Collectively, this morphologic evidence implicates *Slit2* and *Ntn1* in
329 proper ventricular septation during heart development.
330
331 As *Slit2* and *Ntn1* were necessary for ventricular septation, we asked if loss of *Slit2* or *Ntn1* might
332 disturb distribution of the Tbx5^{+}/Mef2cAHF^{+} lineage in the IVS. In homozygous *Slit2* LOF mutants
333 with the lineage reporter (*Tbx5*$^{CreERT2/+}$;*Mef2cAHF-DreERT2*;*ROSA26*$^{Ai66/+}$;*Slit2*$^{-/-}$) (n=4), we
334 observed a statistically-significant broadened distribution of the Tbx5^{+}/Mef2cAHF^{+} lineage
335 compared to controls (n=2) (Figure 6N-Q), consistent with lineage mixing from boundary
336 disruption and implicating a role for SLIT2 in maintaining boundary integrity. Conversely,

337 homozygous *Ntn1* LOF mutants with the lineage reporter (*Tbx5*$^{CreERT2/+}$;*Mef2cAHF-DreERT2*;
338 *ROSA26*$^{Ai66/+}$;*Ntn1*$^{-/-}$) (n=6) demonstrated leftward displacement of the Tbx5^{+}/Mef2cAHF^{+} lineage
339 compared to controls (n=4) (Figure 6R-U), implying that NTN1 signaling precisely positions the
340 compartment boundary at the IVS. Taken together, this evidence suggested that SLIT2- and
341 NTN1-signaling, as part of a Tbx5-dependent pathway, regulates the position and integrity of the
342 compartment boundary labeled by the *Tbx5*$^{+}$*/Mef2cAHF*$^{+}$ lineage.

343

344 **Discussion.**

345 We show that *Tbx5*$^{+}$/*Mef2cAHF*$^{+}$ progenitors prefigure a compartment boundary that becomes
346 located at the junction between the left and right sides of the IVS, providing a cellular framework
347 during development for heart patterning. Our study underscores a fundamental principle that early
348 developmental events preconfigure structure and function of the heart and are susceptible to
349 genetic risks that cause CHDs. Further, our results demonstrate developmental regulation of a
350 compartment boundary by a disease-associated TF and that aberrant tissue patterning from
351 boundary disturbances may be an etiology of birth defects. This study reiterates the importance
352 of compartment boundaries in tissue patterning, provides evidence for compartment boundary
353 disruptions as an etiology of birth defects, and adds to the few examples of compartment
354 boundaries that exist in mammals.

355 We surmise that the rarity of compartment boundaries in mammals likely stems from a few
356 reasons. The discovery of a compartment boundary was first made by studying the fate of marked
357 mosaic cells and their clonal segregation in the wing disk of the fly embryo [36]. Subsequent
358 examples of compartment boundaries were identified by broad genetic screens in Drosophila [37].
359 In mammals, compartment boundaries were discovered by lineage analysis informed by another
360 organism [16] or serendipitously [13], as we have done here. Compartment boundaries have been
361 defined by several criteria. First, a compartment boundary segregates juxtaposed cell populations
362 such as distinct cell lineages to restrict cell intermingling, and ablation of the boundary leads to

363 cell mixing. Second, the expression domain of a selector gene corresponds with a compartment
364 domain, loss of the selector gene eliminates the identity in this territory, and ectopic expression
365 of the selector induces this identity. Third, a selector gene establishes a signaling center to
366 maintain the compartments and boundary. Our results satisfy all of these criteria: Ablation of the
367 *Tbx5*$^{+}$/*Mef2cAHF*$^{+}$ lineage disrupts segregation of *Tbx5*$^{+}$ lineage cells in the LV from the *Tbx5*$^{-}$
368 lineage in the RV of the developing heart. Reduced *Tbx5* expression impairs the integrity of the
369 boundary and its patterning, and in previous work misexpression of TBX5 eliminates IVS
370 formation [25]. Third, TBX5 patterns signaling molecules that are important for morphologies that
371 impact the boundary. In this context, we postulate that *Tbx5* may function as a candidate selector
372 gene. Further experiments will be needed to formally ascertain this.

373 In this context, we identify a *Tbx5*-dependent pathway that regulates *Slit2* and *Ntn1*.
374 Normally, TBX5 represses their ectopic expression in the IVS and compact layer. Both SLIT2 and
375 NTN1 are guidance or adhesive cues in several developmental contexts. Here, we provide
376 evidence that *Slit2* and *Ntn1* are direct targets of TBX5, and that *Tbx5* and *Slit2* or *Ntn1* genetically
377 interact. Further, we found that *Slit2* and *Ntn1* are essential for proper ventricular septation, as
378 well as compartment boundary integrity and positioning, respectively. Like TBX5, proper
379 ventricular septation may be sensitive to imbalanced dosage of SLIT2 or NTN1. As *Ntn1*
380 expression is enriched in the LV and left-side of the IVS in the *Tbx5*$^{+}$ compartment, we propose
381 a working hypothesis that NTN1 functions as a TBX5-dependent signaling center for compartment
382 boundary regulation.

383 The spatiotemporal position of the boundary is at the crux of cardiac septation and, when
384 disrupted, spans sites for congenital cardiac anomalies. The sensitivity of the *Tbx5*$^{+}$/*Mef2cAHF*$^{+}$
385 lineage-labeled boundary to genetic perturbations, specifically *Tbx5* deficiency, is of significance
386 in the context of congenital heart disease. Such deficiency selectively compromises the
387 boundary's integrity and position, along with disturbances to cell orientation, leading to VSDs or
388 AVSDs. This observation suggests that genetic pathways for patterning, like the

389 *Tbx5*$^{+}$/*Mef2cAHF*$^{+}$ lineage-labeled boundary, can be exceptionally susceptible to genetic
390 disruptions. This provides a potential "beacon" for understanding the cellular basis of septation
391 defects. Whether additional genetic perturbations that cause VSDs or AVSDs disrupt the
392 compartment boundary remains to be determined. Likewise, it will be interesting to evaluate if the
393 *Tbx5*$^{+}$/*Mef2cAHF*$^{+}$ lineage-labeled boundary corresponds with abnormal shifts in IVS position, like
394 those observed in the endothelial loss of *Hand2*, which displays rightward shifted IVS and double
395 inlet left ventricle (DILV) or two IVS primordia [38,39].

396 Broadly, our research demonstrates the delicate interplay of progenitor cell behavior, gene
397 expression and compartment boundary formation that determines heart development and genetic
398 susceptibility that increases the risk of CHDs. This evidence further underscores the significance
399 of early developmental stages for the ontogeny of some CHDs. The implications of these
400 discoveries likely extend beyond cardiac morphogenesis, as these findings offer insights for the
401 roles of compartment boundaries during mammalian development and uncover a vulnerability for
402 organ patterning from genetic disturbances.

403

404 **METHODS.**

405 **Mouse lines.** All mouse protocols were approved by the Institutional Animal Care and Use
406 Committee at UCSF. Mice were housed in a barrier animal facility with standard husbandry
407 conditions at the Gladstone Institutes. Mice of *Tbx5*^{CreERT2IRES2xFLAG} (abbreviated here as
408 *Tbx5*^{CreERT2}) and *Mef2cAHF-DreERT2* [6], *Tbx5*$^{del/+}$ and *Tbx5*$^{flox/+}$ [23], *ROSA26*^{Ai66} and *ROSA26*^{Ai6} [18]
409 were described previously. *Mef2cAHF-Cre*$^{/+}$ mice [24] were obtained from Brian Black. *Slit2*$^{+/-}$ mice
410 (MMRC, Strain 065588-UCD, donated by Kent Lloyd) were generated by CRISPR/Cas9-
411 targeted constitutive deletion of exon 8 and flanking splicing regions of *Slit2*. *Ntn1*$^{+/-}$ mice
412 were derived from matings of *Ntn1* floxed mice (*Ntn1*$^{flox/+}$; Jackson Laboratory #028038) [40]
413 to beta-actin-Cre [34], which were obtained from Gail Martin. All mouse strains were maintained
414 in the C57BL6/J background (Jackson Laboratory #664), except for *Tbx5*$^{del/+}$, which was

415 maintained in Black Swiss (Charles River, Strain Code 492), and *Slit2*$^{+/-}$ which was maintained in
416 C57BL6/N (Jackson Laboratory, #005304). Both male and female embryos were collected from
417 timed matings and used at random for experiments. Tamoxifen (Sigma-Adrich; T5648) is
418 suspended in sesame oil at 10mg/mL. The injected dose is 100ug/1 gram of body weight.
419
420 **Cloning and generation of mouse lines.** We generated an attenuated diptheria toxin (DTA176)
421 transgenic knock-in mouse under the control of the dual-recombinase intersectional cassette.
422 DTA176 encodes an attenuated form of toxic fragment A from diptheria toxin [19], which requires
423 ~100-200 molecules for cell killing. This strategy was an effort to reduce potential problems of
424 leaky DTA expression prior to recombinase-mediated activation. Briefly, DTA176 [19] was cloned
425 downstream of ROX-STOP-ROX and LOX-STOP-LOX sites to create a Dre- and Cre-dependent
426 expression construct, which was derived from the Dre- and Cre-dependent tdTomato expression
427 cassette of the Ai66 (RCRL-tdT) targeting vector [18]. After the tdTomato cassette was removed
428 using MluI sites and replaced by DTA176, the construct was cloned into the TARGATT targeting
429 construct pBT346.3 (Applied Stem Cells) to target the transcriptionally inactive *Hip11* locus [41]
430 using PacI and SmaI restriction enzyme sites. The final construct was verified using restriction
431 digestion and Sanger sequencing. DNA was purified and injected along with mRNA for the Phi31o
432 transposase according to manufacturer's protocol to generate intersectional-DTA mutant
433 (*Hip11*$^{Rox\text{-}STOP\text{-}Rox\text{-}Lox\text{-}STOP\text{-}Lox\text{-}DTA176}$) mice. To generate Ai66b mice (*ROSA26*^{Ai66b}), which is a Dre-
434 dependent tdTomato reporter, the LOX-STOP-LOX sites were removed from the Ai66 (RCRL-
435 tdT) targeting vector [18], and then the transgene cassette was inserted into endogenous genomic
436 loci via homologous recombination, as previously described [42].
437
438 **Whole mount embryo and heart immunofluorescence labeling**. Embryos were dissected from
439 timed pregnant dams, including removal of yolk sac for genotyping, as previously described [6].
440 Embryos up to E10.5 were fixed for 4 hours in 4% PFA at room temperature, then incubated with

441 gentle rocking in clearing solution (8% SDS in 0.2M borate buffer) at 37°C for 1-3 hours until clear.
442 E13.5 or E14.5 hearts were micro-dissected from freshly harvested embryos in PBS with heparin
443 (10 Units/mL) (Sigma #H3393) or incubated in 1X RBC lysis solution (Roche #11814389001) for
444 10 minutes at room temperature, fixed at room temperature in 4% PFA for one hour, and
445 incubated with gentle rocking in clearing solution at 37°C for 2-4 days until clear. Specimens were
446 permeabilized and blocked for two hours to overnight with gentle rocking at 37°C in blocking buffer
447 (PBS containing 5% normal donkey serum and 0.8% to 1.5% Triton X-100, dependent on
448 embryo/heart stage). Specimens were labeled with primary antibody (list below) in blocking buffer
449 with gentle rocking at 37°C, either overnight for embryos up to E10.5, or 5 days for E13.5 or E14.5
450 hearts. For long incubations, antibody solution was replaced halfway. Following three washes in
451 blocking buffer, each 45 minutes except the third overnight for E13.5 and E14.5 hearts, specimens
452 were incubated with secondary antibody (raised in donkey; AF488-, Dy405-, Cy3, or AF647-
453 conjugated; used at 1:750; Jackson ImmunoResearch) and DAPI in blocking buffer with gentle
454 rocking at 37°C, 2-3 hours for embryos up to E10.5, or 5 days for E13.5 or E14.5 hearts. Following
455 three washes in PBS with gentle rocking at 37°C, samples were stored (up to overnight) in PBS
456 with 0.2% sodium azide. Primary antibodies used were: tdTomato (rabbit, Rockland 600-401-379,
457 1:1000), MEF2c (sheep, R&D AF6786, 1:250), TNNT2 (mouse, Thermo MS-295-P, 1:500).
458 Strong ZsGreen fluorescence persisted after clearing and did not require immunolabeling.
459
460 **Lightsheet Image Acquisition.** Images were acquired by lightsheet microscopy, as described
461 previously [43]. Brielfy, specimens were warmed and transferred to 2% low melting point agarose
462 (Fisher BP165-25) in PBS at 37°C, then embedded in glass capillary tubes with paired pistons
463 (Sigma Z328510 paired with BR701938, or Sigma Z328502 paired with BR701934) for embryos,
464 or tip-truncated 1mL syringes (Becton Dickinson) for hearts. After the gel solidified, the capillaries
465 or syringes were suspended specimen-down from 14mL polystyrene tubes sealed with Parafilm.
466 Columns containing the specimen were partially extended into an ample volume optical clearing

467 solution (OCS, EasyIndex EI-Z1001, LifeCanvas) overnight. With immersion in OCS, specimens
468 were rotated and imaged from multi-view whole-volume approach on a Light Sheet Z.1
469 microscope (Carl Zeiss Imaging). One of two objective setups was used: EC Plan Neofluar
470 5X/0.16 with 5X/0.1 pair (hearts), or Clr Plan Neofluar 20X/1.0 paired with 10X/0.2 clearing pair
471 (embryos). Z-stacks were collected at each view angle at the optimal slice thickness
472 determined by Zeiss' Zen software, ranging from 1.42 to 4.95 µm.
473
474 **Image Dataset Preprocessing.** Imaging data was processed, as previously described [43]. All data
475 processing was performed on an 8-core x86-64 desktop PC with 64GB RAM, running Kubuntu
476 20.04 LTS, principally using Fiji software [44]. Acquired light sheet image stacks were subjected to
477 single-view deconvolution using regularized generalized Tikhonov filtering (Parallel Spectral
478 Deconvolution, https://imagej.net/plugins/parallel-spectral-deconvolution) following theoretical
479 PSF calculation using the intersection of Gaussian z-plane illumination with Gibson-Lanni
480 widefield epifluorescence detection patterns [45]. Deconvolved stacks were co-registered, and
481 image volumes were generated for each desired orientation, for each specimen, using Content
482 Based Fusion in BigStitcher [46]. TrackMate [47] and ImageJ 3-D viewer were used for segmentation
483 and visualization of fused volumes.
484
485 **Image Volume Quantification**. Extensive whole-volume quantifications of imaged E14.5 hearts
486 were performed using Fiji and associated plugins, with analysis conducted with R. For assessing
487 the location of fluorescence signal, volumes were downsampled, and 2-dimensional regions of
488 interest (ROIs) corresponding to anatomic structures were manually drawn on each Z-slice, using
489 the DAPI channel. Integrated intensity for each fluorescence channel was programatically
490 measured for each ROI, and counts were normalized to DAPI signal and pooled by anatomic
491 region. For whole-heart quantifications, counts were further normalized to combined Ai6 plus Ai66

492 signal, then averaged across each anatomic region. For orientation assessments, a multi-channel
493 panel of 174 full resolution four-chamber image excerpts, evenly distributed between apical-
494 posterior, apical-anterior, posterior-basal, and posterior-apical IVS, were split by channel
495 (tdTomato or ZsGreen) and blindly sampled. Using automated batch processing, these samples
496 were subjected to background filtering, contrast enhancement, and measurements of orientation
497 distribution and dominant direction (OrientationJ plugin, https://github.com/Biomedical-Imaging-
498 Group/OrientationJ), and of directionality (Directionality plugin,
499 https://github.com/fiji/Directionality). Orientation score distributions were rotated so that dominant
500 direction was set to 0°, with average score (across the panel of images) was plotted as a function
501 of direction, and analyzed by Watson's two-sample test. Individual scores surrounding 0° and 90°
502 were pooled and compared with the Wilcoxon signed-rank test. Directionality coherence scores
503 (across the panel of images) were plotted by genotype and compared with the Wilcoxon signed-
504 rank test.
505
506 **Quantification of right-left position of lineages.** For each E10.5 heart analyzed, five
507 representative coronal optical sections were selected, approximately 20-35 μm apart. For each
508 optical section, the DAPI channel was used to draw five linear profiles spanning the ventricular
509 chambers from right to left. Linear profiles were drawn such that the "0" position corresponded to
510 the midline, identified by the interventricular groove. Fluorescence intensity of each channel
511 (green=*Tbx5*$^{+}$ lineage, magenta=*Mef2cAHF*+ lineage) was measured along each linear profile,
512 and intensity values were normalized to the maximum value along each profile. Profiles for each
513 channel were grouped by experimental condition (WT or DTA), and then the average ± SEM
514 normalized fluorescence intensity profiles were calculated and plotted. Welch's two-sample t-test
515 was used at each position along the right-left axis to determine regions of significant difference in
516 fluorescence intensity of each channel between experimental groups, indicating a change in the
517 distribution of cells of that lineage.

518 For each E13.5-E14.0 heart analyzed, maximum z-projections were generated from
519 optical sections spanning every 50 μm from the anterior to posterior of the heart. For each
520 maximum z-projection, the DAPI and red or magenta (*Tbx5*$^{+}$/*Mef2cAHF*$^{+}$ intersectional lineage)
521 channels were split and background subtraction was performed on the red or magenta channel
522 using a 50-pixel rolling ball radius. The DAPI channel was used to draw three linear profiles (basal,
523 middle, apical) spanning the ventricular chambers from right to left. Linear profiles were drawn
524 such that the "0" position corresponded to the middle of the IVS. Fluorescence intensity of the red
525 or magenta channel was measured along each linear profile, and intensity values were
526 normalized to the maximum value along each profile. Profiles were grouped by experimental
527 condition (*Tbx5*$^{CreERT2/+}$ or *Tbx5*$^{CreERT2/flox}$) or (e.g. WT, *Ntn1*$^{+/-}$, *Ntn1*$^{-/-}$) and then the average ± SEM
528 normalized fluorescence intensity profiles were calculated and plotted. Two sample F-test and
529 Welch's t-test were used to analyze the distribution of *Tbx5*$^{+}$/*Mef2cAHF*$^{+}$ intersectional lineage
530 cells.
531
532 **Cell Harvesting for Single Cell RNA Sequencing**. Samples for single cell RNA sequencing
533 were collected from three independent litters at E13.5. The heart was microdissected to obtain
534 the interventricular septum (IVS), left ventricular (LV) and right ventricular (RV) regions. Control
535 samples were *Tbx5*$^{CreERT2/+}$*;Mef2cAHF-DreERT2;ROSA26*$^{Ai66/Ai6}$ (n=3) and
536 *Tbx5*$^{CreERT2/+}$*;Mef2cAHF-DreERT2;ROSA26*$^{Ai66/+}$ (n=1) for LV, RV and IVS each. *Tbx5* mutant
537 samples were *Tbx5*$^{CreERT2/flox}$*;Mef2cAHF-DreERT2;ROSA26*$^{Ai66/Ai6}$ for RV and LV (n=3 each) and
538 IVS (n=2).
539 Each microdissected tissue was singularized with TrypLE Express (Life Technologies,
540 Cat# 12604-013) at 37C and quenched with 1% FBS in PBS. The single cell suspension was then
541 filtered through a cell strainer cap (Corning, Cat# 352235) and centrifuged at 300g for 5 minutes.
542 The pellet was resuspended in 1% FBS in PBS and counted using an automated cell counter. A
543 30μL aliquot of the cell suspension was used to generate single cell droplet libraries with the

544 Chromium Next GEM Single Cell 5' Library & Gel Bead Kit v1.1, according to manufacturer's
545 instructions (10X Genomics). After KAPA qPCR quantification, a shallow sequencing run was
546 performed on a NextSeq 500 (Illumina) prior to deep sequencing on a NovaSeq S4 (Illumina). For
547 control IVS+AVC, at E13.5, 3 samples were *Tbx5*$^{CreERT2/+;}$*Mef2cAHF-DreERT2;ROSA26*$^{Ai66/Ai6}$
548
549 **Data Processing Using Cellranger**. All datasets were processed using Cellranger 2.0.2. FASTQ
550 files were generated using the mkfastq function. Reads were aligned to a custom mm9 reference
551 (version 1.2.0) containing tdTomato and ZsGreen reporter genes. Cellranger aggr was used to
552 aggregate individual libraries after read depth normalization.
553
554 **Seurat Analysis**. Outputs from the Cellranger pipeline were analyzed using the Seurat v3 [48–50].
555 Datasets from the IVS, LV and RV were analyzed separately. Cells with 10,000-50,000 UMIs and
556 1500-7250 genes were retained. Data was normalized using the NormalizeData function and
557 scaled using ScaleData, while also regressing unwanted sources of variation, such as differences
558 in the number of UMIs, number of genes, percentage of mitochondrial reads and differences
559 between G2M and S phase scores. Principal component analysis (PCA) was performed using the
560 most highly variable genes. Cells were then clustered based on the top 30 principal components
561 and visualized on a Uniform Manifold Approximation and Projection (UMAP) [51]. A clustering
562 resolution that separated cells by major cell types was chosen. Next, *Tnnt2*$^{+}$ clusters from the IVS
563 dataset were extracted and re-clustered, similar to the parent dataset above. A clustering
564 resolution was chosen based on separation of genotypes. Differential gene expression tests
565 between clusters or between *ZsGreen*$^{+}$ and *ZsGreen*$^{-}$ or *tdTomato*$^{+}$ and *tdTomato*$^{-}$ cells were
566 performed using the FindMarkers function with default parameters. Selected differentially
567 expressed genes with an adjusted p-value less than 0.05 from the Wilcoxon rank sum test were
568 displayed using the Dotplot or FeaturePlot functions.
569

570 **Fluorescent *In Situ* Hybridization.** E11.5 or E14.5 hearts were fixed with 4% paraformaldehyde
571 or 10% formalin overnight at 4C, embedded in paraffin and then sectioned for a transverse or
572 four-chambered view on slides. *In situ* hybridization was performed on sections using the
573 RNAscope Multiplex Fluorescent v2 Assay kit (Advanced Cell Diagnostics, Cat# 323100). Briefly,
574 sections were deparaffinized in xylene and 100% ethanol, treated with hydrogen peroxide for 10
575 minutes and boiled in target retrieval buffer for 10 minutes. A hydrophobic barrier was drawn
576 around each section using an Immedge pen (Vector Laboratories, Cat# H-4000), and slides were
577 allowed to dry overnight. The following day, sections were treated with Protease Plus for 30
578 minutes, followed by hybridization with probes for 2 hours at 40C. Probes used were *Mm-Tnnt2-*
579 *C4* (Cat# 418681-C4), *Mm-Ntn1* (Cat# 407621), *Mm-Slit2* (Cat# 449691), *Mm-Nppa-C3* (Cat#
580 418691-C3), *Mm-Bmp2-C2* (Cat# 406661-C2), *Mm-Robo1* (Cat# 475951) and *Mm-Unc5b* (Cat#
581 482481). Amplification steps were carried out according to manufacturer's instructions. Opal dyes
582 520, 570, 620 and 690 (Akoya Biosciences, Cat# FP1487001KT, FP1487001KT, FP1487001KT
583 and FP1487001KT) were used at 1:750 dilution. After staining with DAPI, 1-2 drops of ProLong
584 Gold Antifade Mountant (ThermoFisher Scientific, Cat# P36930) were placed on the slides and
585 mounted with a coverslip. Slides were stored overnight at 4C and were imaged at 10X
586 magnification on the Olympus FV3000RS. Multi-Area Time Lapse (MATL) images were captured
587 and then stitched together using the Olympus FV3000RS software. Stitched images were
588 analyzed using ImageJ OlympusViewer plugin.
589
590 **Immunohistochemistry.** Cryopreserved slides were thawed from -80C at RT and washed in
591 0.1% Triton X-100 in PBS (PBST) for 3 x 5 min. Antigen-retrieval was performed by boiling
592 slides in 10mM sodium citrate buffer (pH 6.0) for 10 minutes and then washed in H2O for 3 x 5
593 min. Blocking was performed using 5% donkey serum in 0.1% PBST at RT for 1-2hr. Anti-
594 Netrin-1 antibody 1:500 (R&D Systems AF1109) in 1% BSA + 0.1% PBST was incubated at 4C
595 overnight. After washing 3 x 5 min in 0.1% PBST, slides incubated in Alexa Fluor 594 (1:300) in

596 1% BSA + 0.1% PBST at RT for 1 hr. Slides were then washed 3 x 5 min in 0.1% PBST and
597 incubated in 1:1000 DAPI in 0.1% PBST at RT for 5-10 minutes. Finally, slides washed 3 x 5
598 min in 0.1% PBST, glass coverslips were mounted using Prolong Gold antifade mounting
599 medium and stored at 4C.
600
601 **Machine learning-based 3-D reconstruction from histology and quantitative micrometry.**
602 Tissues were formalin-fixed, paraffin embedded (FFPE) and serially sectioned at a standard
603 thickness of 5 μm to exhaustively collect the heart tissue of each fetal mouse. Serial sections
604 were stained with hematoxylin and eosin (H&E) and digitized at 20x magnification. CODA, a
605 technique to 3-D reconstruct serial tissue images, was used to map the microanatomy of the
606 hearts [35,52]. The various steps of CODA can be broken down into image registration, nuclear
607 detection, and tissue labelling. Nonlinear image registration was used to align the serial images.
608 Cellular coordinates were generated through color deconvolution and detection of two-
609 dimensional intensity peaks in the hematoxylin channel of the images. A deep learning semantic
610 segmentation algorithm was trained to label the anatomical structures of the mice at 1 μm
611 resolution. To train the model, manual annotations of six structures were generated in 55
612 histological images corresponding to the different large structures present in the tissue: bones,
613 spinal cord, lung, liver, stroma, heart, and non-tissue pixels in the images. A second deep learning
614 model was trained to subclassify the regions of interest within the heart: compact myocardium,
615 trabeculae, IVS, AV canal and atria. Fifty images from the manual annotation datasets were used
616 for model training, with five images held out for independent testing of model accuracy. The
617 models were deemed acceptable when they reached a minimum per-class precision and recall of
618 >85%. Using the trained model, independent images were segmented and aligned to generate
619 digital 3-D datasets.
620 The reconstructed volumes enabled microanatomical quantification of anatomical
621 properties. IVS fill, or the solidity of the muscle layer in the IVS, was calculated by dividing the

number of dark (<200 in RBG color space) pixels within the IVS, normalized by all pixels (including empty space) within the IVS. Percent trabeculation within the IVS was calculated by first isolating the tissue classified as trabeculae that was spatially attached to the IVS, then normalizing this number by the combined volume of trabeculae attached to IVS and the volume of the IVS itself. The compact myocardium thickness was calculated by measuring the thickness of the compact layer at the bottom 20% of the ventricles. To measure the thickness on the left and right ventricles, the two sides of the heart were manually segmented in 3-D space. VSDs were identified by calculating regions where the empty space of the left ventricle contacted the empty space of the right ventricle. These defects were evaluated and manually sorted into membranous or muscular sub-types. The areas of each defect were then manually calculated through annotation on serial histological images representing the shortest path to close the defect. These lines were summed across all images containing the defect multiplied by the thickness of the histological slides to determine the area of the hole.

Quantification and Statistical Analysis. For statistical analysis of genetic interactions, the number of animals with a given defect (muscular VSD or membranous VSD) was modeled in a Generalized Linear Model assuming a binomial probability distribution for the observed counts. This model included main effects (in terms of log odds ratios) capturing the number of mutant alleles for *Tbx5* (0 or 1, representing the WT or the Het genotype, respectively) and the number of mutant alleles for *Slit2* or *Ntn1* (0,1 or 2: representing the WT, Het or Hom genotype, respectively) and an interaction between these effects. Given the relatively small number of animals in this experiment, bias-reduced estimates were made using the brglm2 package {Kosmidis.2020} in R <https://www.R-project.org/>.

References.

647 1. de la Cruz, M. V., Sánchez-Gómez, C. & Palomino, M. A. The primitive cardiac regions in the
648 straight tube heart (Stage 9) and their anatomical expression in the mature heart: An
649 experimental study in the chick embryo. *J. Anat.* **165**, 121–31 (1989).

650 2. de la Cruz, M. V., Castillo, M. M., G., L. V., Valencia, A. & Moreno-Rodriguez, R. A. Primitive
651 interventricular septum, its primordium, and its contribution in the definitive interventricular
652 septum: In vivo labelling study in the chick embryo heart. *Anatomical Rec* **247**, 512–520 (1997).

653 3. Wessels, A. *et al.* Spatial distribution of “tissue-specific” antigens in the developing human
654 heart and skeletal muscle. I. An immunohistochemical analysis of creatine kinase isoenzyme
655 expression patterns. *Anatomical Rec* **228**, 163–176 (1990).

656 4. Wessels, A. *et al.* The Development of the Atrioventricular Junction in the Human Heart. *Circ*
657 *Res* **78**, 110–117 (1996).

658 5. Lamers, W. H. *et al.* New findings concerning ventricular septation in the human heart.
659 Implications for maldevelopment. *Circulation* **86**, 1194–1205 (2018).

660 6. Devine, W. P., Wythe, J. D., George, M., Koshiba-Takeuchi, K. & Bruneau, B. G. Early
661 patterning and specification of cardiac progenitors in gastrulating mesoderm. *eLife* **3**, 508
662 (2014).

663 7. Später, D. *et al.* A HCN4+ cardiomyogenic progenitor derived from the first heart field and
664 human pluripotent stem cells. *Nat Cell Biol* **15**, 1–10 (2013).

665 8. Lescroart, F. *et al.* Early lineage restriction in temporally distinct populations of Mesp1
666 progenitors during mammalian heart development. *Nat Cell Biol* **16**, 829–840 (2014).

667 9. Meilhac, S. M., Esner, M., Kelly, R. G., Nicolas, J.-F. & Buckingham, M. E. The clonal origin
668 of myocardial cells in different regions of the embryonic mouse heart. *Dev Cell* **6**, 685–698
669 (2004).

670 10. Kiecker, C. & Lumsden, A. Compartments and their boundaries in vertebrate brain
671 development. *Nat Rev Neurosci* **6**, 553–564 (2005).

672 11. Dahmann, C., Basler, K., Dahmann, C. & Basler, K. Compartment boundaries: at the edge
673 of development. *Trends Genet* **15**, 320–326 (1999).

674 12. Wang, J. & Dahmann, C. Establishing compartment boundaries in Drosophila wing imaginal
675 discs: An interplay between selector genes, signaling pathways and cell mechanics. *Semin Cell*
676 *Dev Biol* **107**, 161–169 (2020).

677 13. Kimmel, R. A. *et al.* Two lineage boundaries coordinate vertebrate apical ectodermal ridge
678 formation. *Genes Dev.* **14**, 1377–1389 (2000).

679 14. Arques, C. G., Doohan, R., Sharpe, J. & Torres, M. Cell tracing reveals a dorsoventral
680 lineage restriction plane in the mouse limb bud mesenchyme. *Development* **134**, 3713–3722
681 (2007).

682 15. Qiu, Q., Chen, H. & Johnson, R. L. Lmx1b-expressing cells in the mouse limb bud define a
683 dorsal mesenchymal lineage compartment. *Genesis* **47**, 224–233 (2009).

684 16. Zervas, M., Millet, S., Ahn, S. & Joyner, A. L. Cell Behaviors and Genetic Lineages of the
685 Mesencephalon and Rhombomere 1. *Neuron* **43**, 345–357 (2004).

686 17. Franco, D. *et al.* Left and right ventricular contributions to the formation of the
687 interventricular septum in the mouse heart. *Dev Biol* **294**, 366–375 (2006).

688 18. Madisen, L. *et al.* Transgenic Mice for Intersectional Targeting of Neural Sensors and
689 Effectors with High Specificity and Performance. *Neuron* **85**, 942–958 (2015).

690 19. Wu, S., Wu, Y. & Capecchi, M. R. Motoneurons and oligodendrocytes are sequentially
691 generated from neural stem cells but do not appear to share common lineage-restricted
692 progenitors in vivo. *Development* **133**, 581–590 (2006).

693 20. Basson, C. T. *et al.* Mutations in human TBX5 [corrected] cause limb and cardiac
694 malformation in Holt-Oram syndrome. *Nat Genet* **15**, 30–35 (1997).

695 21. Li, Q. Y. *et al.* Holt-Oram syndrome is caused by mutations in TBX5, a member of the
696 Brachyury (T) gene family. *Nat Genet* **15**, 21–29 (1997).

697 22. Kathiriya, I. S. *et al.* Modeling Human TBX5 Haploinsufficiency Predicts Regulatory
698 Networks for Congenital Heart Disease. *Dev Cell* **56**, 292-309.e9 (2021).

699 23. Bruneau, B. G. *et al.* A murine model of Holt-Oram syndrome defines roles of the T-box
700 transcription factor Tbx5 in cardiogenesis and disease. *Cell* **106**, 709–721 (2001).

701 24. Verzi, M. P., McCulley, D. J., Val, S. D., Dodou, E. & Black, B. L. The right ventricle, outflow
702 tract, and ventricular septum comprise a restricted expression domain within the
703 secondary/anterior heart field. *Dev Biol* **287**, 134–145 (2005).

704 25. Koshiba-Takeuchi, K. *et al.* Reptilian heart development and the molecular basis of cardiac
705 chamber evolution. *Nature* **461**, 95–98 (2009).

706 26. Xie, L. *et al.* Tbx5-Hedgehog Molecular Networks Are Essential in the Second Heart Field
707 for Atrial Septation. *Dev Cell* **23**, 280–291 (2012).

708 27. Mori, A. D. & Bruneau, B. G. TBX5 mutations and congenital heart disease: Holt-Oram
709 syndrome revealed. *Curr Opin Cardiol* **19**, 211–215 (2004).

710 28. Mommersteeg, M. T. M., Yeh, M. L., Parnavelas, J. G. & Andrews, W. D. Disrupted Slit-
711 Robo signalling results in membranous ventricular septum defects and bicuspid aortic valves.
712 *Cardiovasc Res* **106**, 55–66 (2015).

713 29. Li, Y. *et al.* Global genetic analysis in mice unveils central role for cilia in congenital heart
714 disease. *Nature* **521**, 1–16 (2015).

715 30. Kruszka, P. *et al.* Loss of function in ROBO1 is associated with tetralogy of Fallot and septal
716 defects. *J Med Genet* **54**, 825 (2017).

717 31. Larrieu-Lahargue, F., Thomas, K. R. & Li, D. Y. Netrin Ligands and Receptors: Lessons
718 From Neurons to the Endothelium. *Trends Cardiovas Med* **22**, 44–47 (2012).

719 32. Akerberg, B. N. *et al.* A reference map of murine cardiac transcription factor chromatin
720 occupancy identifies dynamic and conserved enhancers. *Nat Commun* **10**, 4907 (2019).

721 33. Bin, J. M. *et al.* Complete Loss of Netrin-1 Results in Embryonic Lethality and Severe Axon
722 Guidance Defects without Increased Neural Cell Death. *CellReports* **12**, 1099–1106 (2015).

723 34. Lewandoski, M., Meyers, E. N. & Martin, G. R. Analysis of Fgf8 gene function in vertebrate
724 development. *Cold Spring Harb Sym* **62**, 159–68 (1997).

725 35. Kiemen, A. L. *et al.* CODA: quantitative 3D reconstruction of large tissues at cellular
726 resolution. *Nat Methods* 1–10 (2022) doi:10.1038/s41592-022-01650-9.

727 36. Vincent, J. P. Compartment boundaries: where, why and how? *Int. J. Dev. Biol.* **42**, 311–5
728 (1998).

729 37. Lawrence, P. A. & Struhl, G. Morphogens, compartments, and pattern: lessons from
730 drosophila? *Cell* **85**, 951–961 (1996).

731 38. VanDusen, N. J. *et al.* Hand2 Is an Essential Regulator for Two Notch-Dependent Functions
732 within the Embryonic Endocardium. *Cell Rep.* **9**, 2071–2083 (2014).

733 39. George, R. M. *et al.* Single cell evaluation of endocardial HAND2 gene regulatory networks
734 reveals critical HAND2 dependent pathways impacting cardiac morphogenesis. *Development*
735 **150**, (2023).

736 40. Bin, J. M. *et al.* Complete Loss of Netrin-1 Results in Embryonic Lethality and Severe Axon
737 Guidance Defects without Increased Neural Cell Death. *Cell Reports* **12**, 1099–1106 (2015).

738 41. Tasic, B. *et al.* Site-specific integrase-mediated transgenesis in mice via pronuclear
739 injection. *Proc National Acad Sci* **108**, 7902–7907 (2011).

740 42. Madisen, L. *et al.* A robust and high-throughput Cre reporting and characterization system
741 for the whole mouse brain. *Nat Neurosci* **13**, 133–140 (2010).

742 43. Dominguez, M. H., Krup, A. L., Muncie, J. M. & Bruneau, B. G. Graded mesoderm assembly
743 governs cell fate and morphogenesis of the early mammalian heart. *Cell* **186**, 479-496.e23
744 (2023).

745 44. Schindelin, J. *et al.* Fiji: an open-source platform for biological-image analysis. *Nat. Methods*
746 **9**, 676–682 (2012).

747 45. Kirshner, H., Aguet, F., Sage, D. & Unser, M. 3-D PSF fitting for fluorescence microscopy:
748 implementation and localization application. *J. Microsc.* **249**, 13–25 (2013).

46. Hörl, D. *et al.* BigStitcher: reconstructing high-resolution image datasets of cleared and expanded samples. *Nat Methods* **16**, 870–874 (2019).

47. Tinevez, J.-Y. *et al.* TrackMate: An open and extensible platform for single-particle tracking. *Methods* **115**, 80–90 (2017).

48. Satija, R., Farrell, J. A., Gennert, D., Schier, A. F. & Regev, A. Spatial reconstruction of single-cell gene expression data. *Nat Biotechnol* **33**, 495–502 (2015).

49. Butler, A., Hoffman, P., Smibert, P., Papalexi, E. & Satija, R. Integrating single-cell transcriptomic data across different conditions, technologies, and species. *Nat Biotechnol* **48**, 1070–17 (2018).

50. Stuart, T. *et al.* Comprehensive Integration of Single-Cell Data. *Cell* **177**, 1–37 (2019).

51. Becht, E. *et al.* Dimensionality reduction for visualizing single-cell data using UMAP. *Nat Biotechnol* (2018) doi:10.1038/nbt.4314.

52. Forjaz, A. *et al.* Three-dimensional assessments are necessary to determine the true spatial tissue composition of diseased tissues. *bioRxiv* 2023.12.04.569986 (2023) doi:10.1101/2023.12.04.569986.

Acknowledgements. We dedicate this manuscript in memory of Tatyana Sukonnik. We thank Brian Black for mouse lines and members of the Bruneau lab for troubleshooting help, discussions and comments. We also thank the Gladstone Bioinformatics, Genomics, and Histology and Microscopy Cores, the UCSF Laboratory for Cell Analysis, and the UCSF Center for Advanced Technology. This work was supported by grants from the National Institutes of Health (NHLBI Bench to Bassinet Program UM1HL098179 to B.G.B.; R01HL114948 to B.G.B., R01HL155906 to B.G.B. and I.S.K., F32 HL162450 to J.M.M-V, U54CA268083 and UG3CA275681 to A.L.K.), Additional Ventures to B.G.B., Society for Pediatric Anesthesia (Young Investigator Award to I.S.K.), Hellman Family Fund (I.S.K.), UCSF REAC Grant (I.S.K.), UCSF Pediatric Heart Center Catalyst Award to I.S.K. and UCSF Department of Anesthesia and Perioperative Care (Ongoing Investigator Award to I.S.K.). This work was also supported by an NIH/NCRR grant (C06 RR018928) to the J. David Gladstone Institutes, and the Younger Family Fund (B.G.B.).

Author Contributions. W.P.D. and B.G.B. originally conceived, and I.S.K. and B.G.B. refined and developed the study. W.P.D. made initial observations using genetic lineage tools that he gathered or generated, such as *ROSA26*^{Ai66b} and the intersectional-*DTA*. I.S.K., M.H.D., W.P.D. and K.M.H. performed embryo dissections. K.M.H., B.I.G., P.G., M.N.M., T.S., D.M.P., S.W. and E.F.B. managed animal husbandry and genotyping. I.S.K., M.H.D., W.P.D. and K.M.H. performed whole mount or section immunostaining experiments and imaging. M.H.D., J.M.M. and D.Q performed lightsheet imaging and processing, and M.H.D. and J.M.M. implemented analyses with hypothesis-based input from I.S.K. I.S.K. designed the strategy to use 5' sequencing kit and developed synthetic genome with Gladstone Bioinformatics core, micro-dissected heart regions for scRNA-seq and processed samples with K.S.R. and P.G. for sequencing library preparations. K.S.R. generated scRNA-seq libraries and performed scRNA-seq analyses with hypothesis-based input from I.S.K. K.S.R., K.M.H., P.G. and M.N.M. performed section *in situ* hybridization and imaging. K.S.R. generated ChIP-seq browser tracks with input from S.K.H. I.S.K. assessed cardiac defects by histology and provided anatomical knowledge to A.L.K. to apply a deep learning tool for cardiac morphometry. A.F. trained deep learning models and was supervised by A.L.K. and advised by P-H.W. and D.W. B.G.B. supervised and advised the study. I.S.K. and K.S.R. prepared figures. I.S.K. wrote the original draft with contributions from co-authors. I.S.K. and B.G.B. reviewed and edited the manuscript with input from co-authors.

Declaration of Interests: B.G.B. is a co-founder and shareholder of Tenaya Therapeutics. B.G.B. is an advisor for Silver Creek Pharmaceuticals. None of the work presented here is related to these commercial interests.

Figure 1

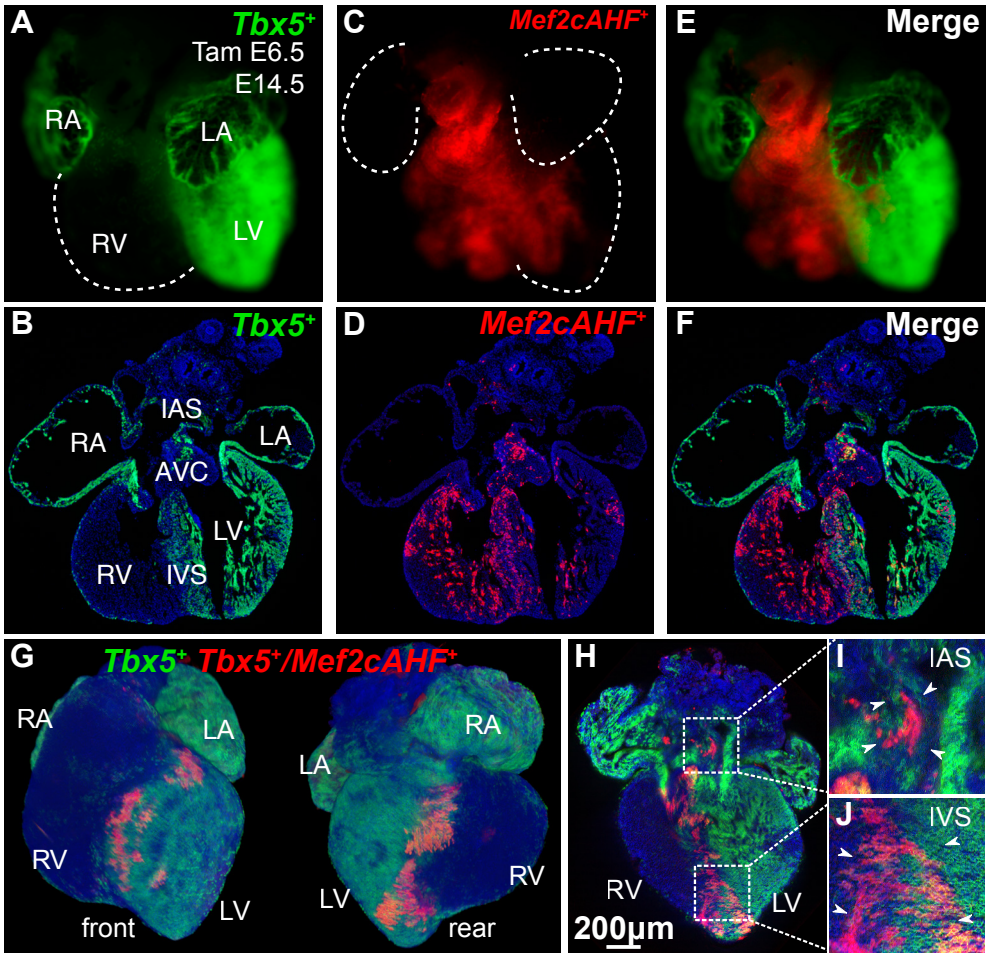
A
Tbx5+
Tam E6.5
E14.5
RA
LA
RV
LV
C
Mef2cAHF+
E
Merge
B
Tbx5+
IAS
RA
LA
AVC
LV
RV
IVS
D
Mef2cAHF+
F
Merge
G
Tbx5+ Tbx5+/Mef2cAHF+
RA
LA
RV
LV
front
RA
LA
RV
LV
rear
H
RV
LV
200µm
I
IAS
J
IVS

Figure 1. *Tbx5*$^{+}$/*Mef2cAHF*$^{+}$ lineage marks a compartment boundary at the cardiac interventricular septum At E14.5, (A, B) clonal cell descendants of a *Tbx5*$^{+}$ lineage (ZsGreen) labeled at E6.5 contributes to the LV, and (C, D) a *Mef2cAHF*$^{+}$ lineage (tdTomato immunostaining) contributes to the RV, demonstrating largely complementary patterns. (F-J) These lineages overlap (*Tbx5*$^{+}$/*Mef2cAHF*$^{+}$) at the interventricular septum (IVS), as well as the atrioventricular canal (AVC) and interatrial septum (IAS). *Tbx5*$^{CreERT2/+}$;*Mef2cAHF-DreERT2*;*ROSA26*$^{Ai6/Ai66b}$ hearts by epifluorescence microscopy (A-C) and cryosections (D-F). (G-J) Maximal projection images by light sheet microscopy of an intersectional reporter for the *Tbx5*$^{+}$/*Mef2cAHF*$^{+}$ lineage (tdTomato immunostaining) in *Tbx5*$^{CreERT2/+}$;*Mef2cAHF-DreERT2*;*ROSA26*$^{Ai66/+}$ embryos.

Figure S1

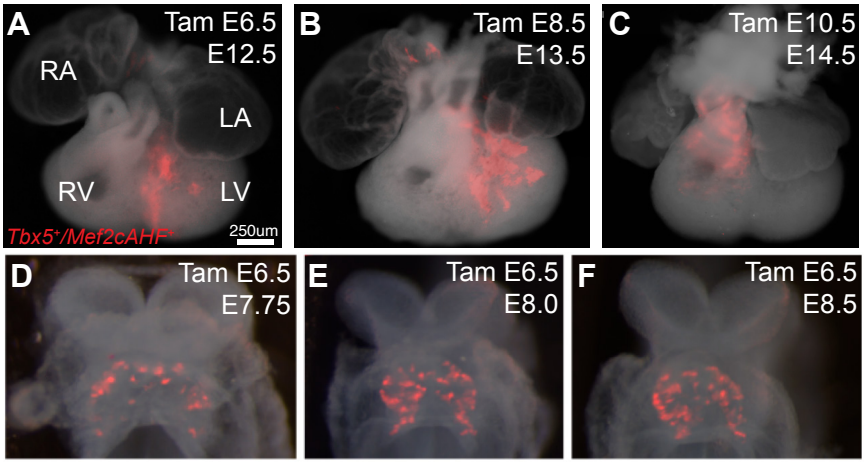
A
Tam E6.5
E12.5
RA
LA
RV
LV
Tbx5+/Mef2cAHF+
250um
B
Tam E8.5
E13.5
C
Tam E10.5
E14.5
D
Tam E6.5
E7.75
E
Tam E6.5
E8.0
F
Tam E6.5
E8.5

814 **Supplemental Figure 1.** (A-C) *Tbx5*$^{+}$*/Mef2cAHF*$^{+}$ lineage contributions to the interventricular
815 septum were descendants from progenitors labeled at (A) E6.5, but not at (B) E8.5 or (C) E10.5
816 in *Tbx5*$^{CreERT2/+}$;*Mef2cAHF-DreERT2*;*ROSA26*$^{Ai6/Ai66}$ embryos. Epifluorescence microscopy
817 images of the *Tbx5*$^{+}$*/Mef2cAHF*$^{+}$ lineage (tdTomato immunostaining) labeled at E6.5 from (A)
818 E7.75, (B) E8.0 and (C) E8.5 displayed an apparent “salt and pepper” pattern in the early
819 developing heart.
820
821

Figure 2

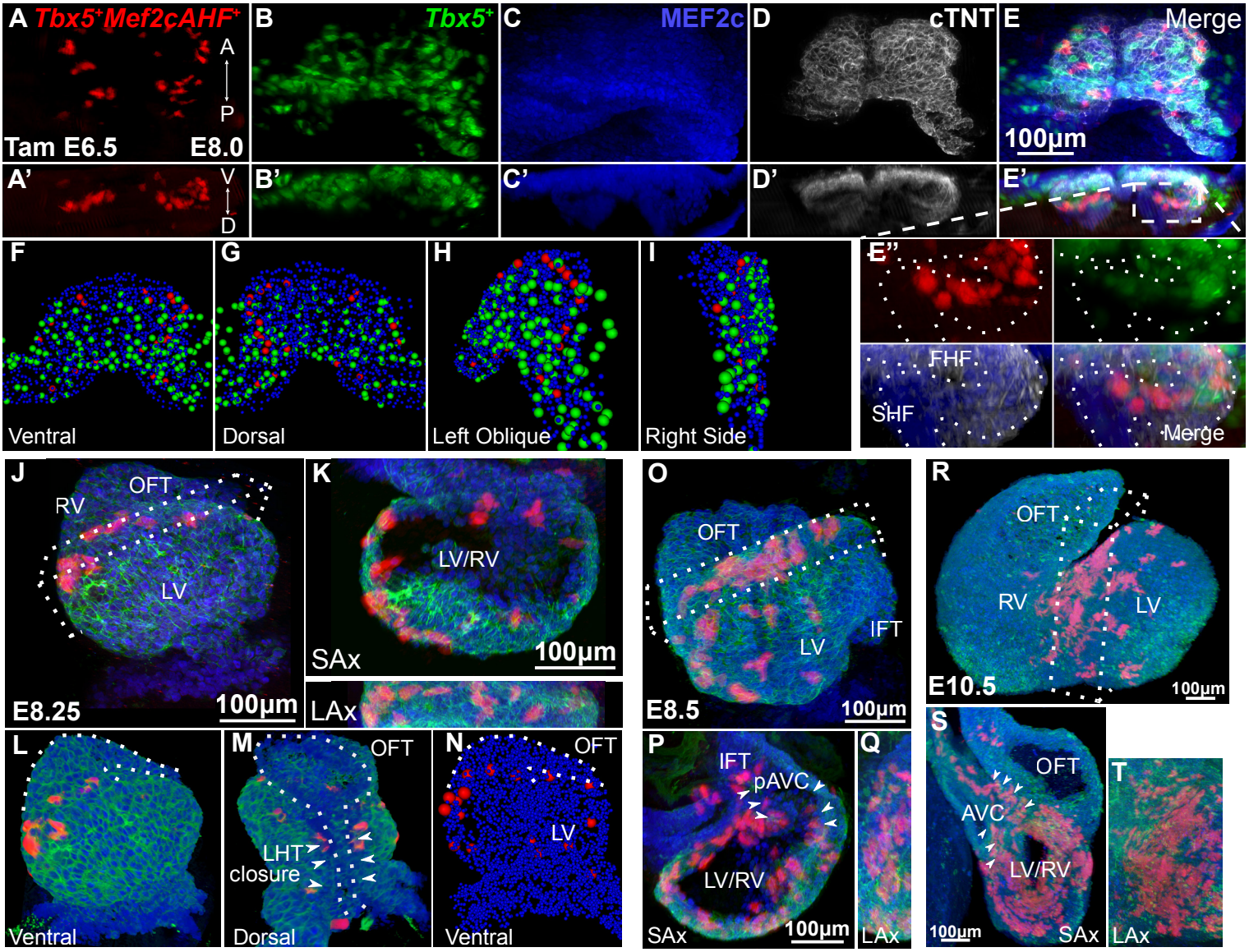
A Tbx5+Mef2cAHF+
A
P
Tam E6.5
E8.0
B Tbx5+
C MEF2c
D cTNT
E Merge
100µm
A'
V
D
B'
C'
D'
E'
F
Ventral
G
Dorsal
H
Left Oblique
I
Right Side
E''
FHF
SHF
Merge
J
OFT
RV
LV
E8.25
100µm
K
LV/RV
SAx
100µm
LAx
O
OFT
IFT
LV
E8.5
100µm
R
OFT
RV
LV
E10.5
100µm
L
Ventral
M
OFT
LHT
closure
Dorsal
N
OFT
LV
Ventral
P
IFT
pAVC
LV/RV
SAx
100µm
Q
LAx
S
OFT
AVC
LV/RV
100µm
SAx
T
LAx

822 **Figure 2. *Tbx5*$^{+}$*/Mef2cAHF*$^{+}$ lineage is prefigured in early mouse heart development.** Frontal
823 (A-E), transverse (A'-E') and magnified transverse (E'') views of maximum Z-projections of whole
824 mount embryos by lightsheet imaging at E8.0 show the *Tbx5*$^{+}$ lineage (ZsGreen), and
825 immunostaining of tdTomato for the *Tbx5*$^{+}$*/Mef2cAHF*$^{+}$ lineage, MEF2c and cTNT in
826 *Tbx5*$^{CreERT2/+}$;*Mef2cAHF-DreERT2*;*ROSA26*$^{Ai6/Ai66}$ embryos. A-P, anterior-posterior axis; V-D,
827 ventral-dorsal axis. First (FHF) and second (SHF) heart fields. At E8.0 (approximately 3 somites),
828 *Tbx5*$^{+}$ lineage cells are restricted to a ventral domain corresponding to the FHF, whereas
829 *Tbx5*$^{+}$*/Mef2cAHF*$^{+}$ lineage cells originate along the FHF-SHF boundary. *Tbx5*$^{+}$*/Mef2cAHF*$^{+}$
830 lineage cells lie in an apparent planar ringlet in the dorsal-ventral axis that expands as the heart
831 tube grows. (J-N) At E8.25 (approximately 6 somites), with dorsal closure of the linear heart tube
832 (LHT) underway, the *Tbx5*$^{+}$*/Mef2cAHF*$^{+}$ lineage cells form a ring situated between the RV and LV
833 primordia, which is observed from multiple perspectives including anterior, short-axis (SAx) and
834 long-axis (LAx) views. (O-Q) At E8.5 (approximately 9 somites), *Tbx5*$^{+}$*/Mef2cAHF*$^{+}$ lineage cells
835 are observed in a portion of the AVC primoridium (pAVC and arrowheads). (R-T) At E10.5, a band
836 of *Tbx5*$^{+}$*/Mef2cAHF*$^{+}$ lineage cells extends from the interventricular groove at the outer curvature
837 to the inner curvature of the heart. SAx and LAx show that *Tbx5*$^{+}$*/Mef2cAHF*$^{+}$ lineage cells
838 occupies a crossroads for heart morphogenesis, spanning the growing interventricular septum to
839 the AVC, adjacent to the OFT.
840
841

Figure S2

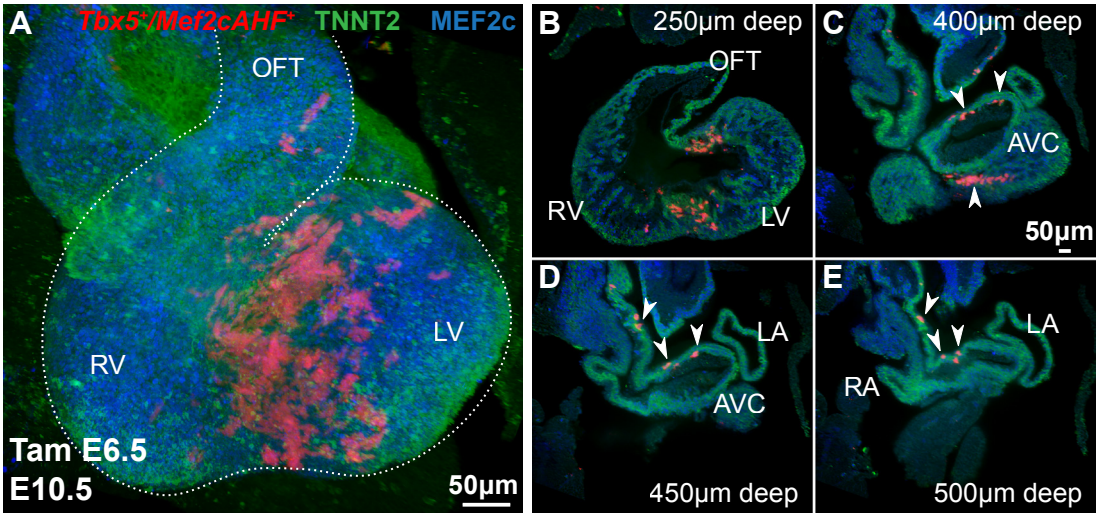
A
Tbx5+/Mef2cAHF+
TNNT2
MEF2c
OFT
RV
LV
Tam E6.5
E10.5
50μm
B
250μm deep
OFT
RV
LV
C
400μm deep
AVC
50μm
D
LA
AVC
450μm deep
E
LA
RA
500μm deep

842 **Supplemental Figure 2.** (A-E) In the developing atria, optical sections from ventral to dorsal show
843 lineage-labeled *Tbx5*$^{+}$/*Mef2cAHF*$^{+}$ lineage cells from the AV cushion (AVC) region to the roof of
844 the atrium, prior to the formation of the interatrial septum, in *Tbx5*$^{CreERT2/+}$;*Mef2cAHF-*
845 *DreERT2*;*ROSA26*$^{Ai6/Ai66}$ embryos.
846
847 **Video 1.** Related to Figure 2 and Supplemental Figure 2.
848
849

Figure 3

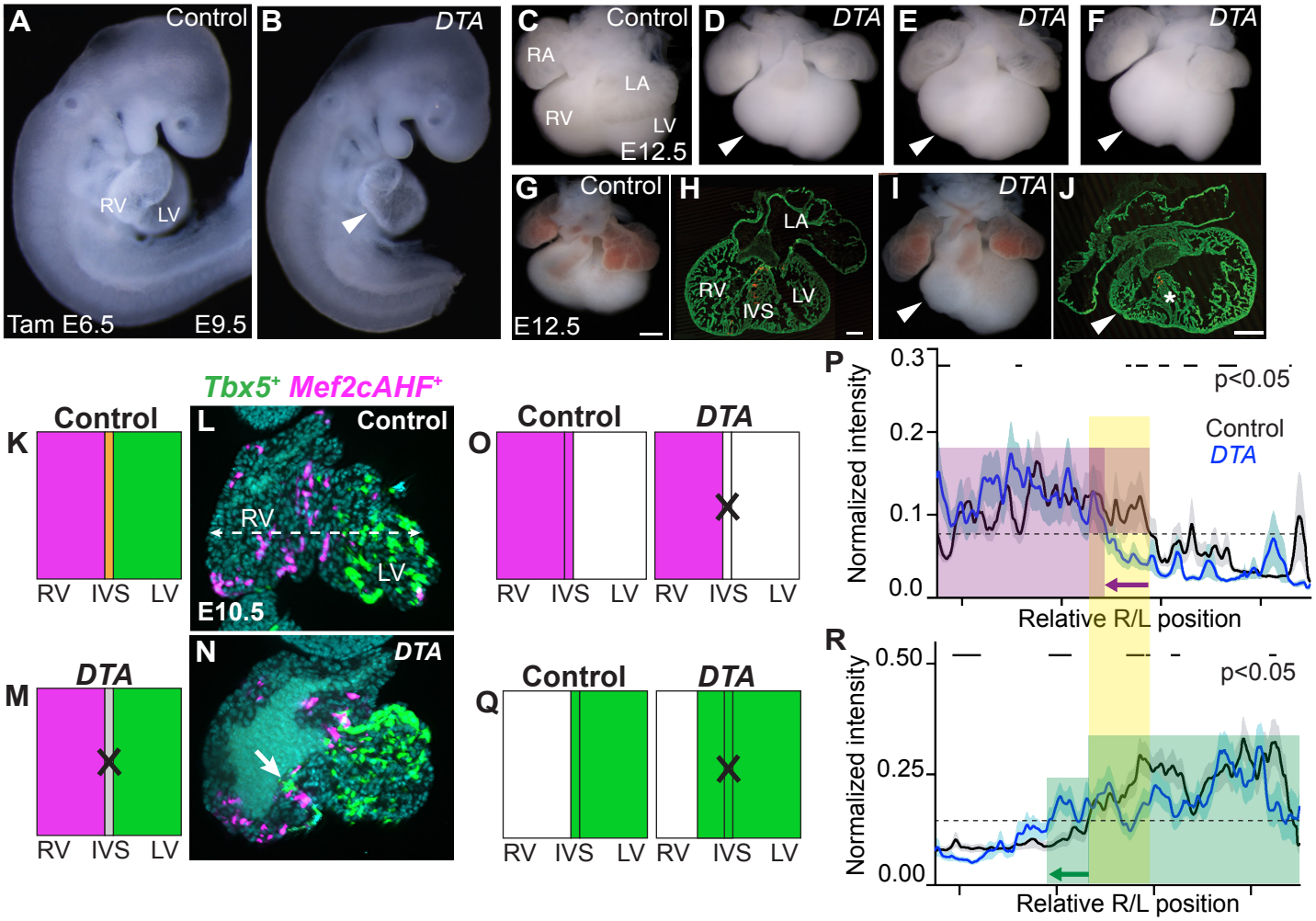
A
Control
RV
LV
Tam E6.5
E9.5
B
DTA
C
Control
RA
LA
RV
LV
E12.5
D
DTA
E
DTA
F
DTA
G
Control
E12.5
H
LA
RV
IVS
LV
I
DTA
J
Tbx5+ Mef2cAHF+
K
Control
RV IVS LV
L
Control
RV
LV
E10.5
M
DTA
RV IVS LV
N
DTA
O
Control
DTA
RV IVS LV RV IVS LV
Q
Control
DTA
RV IVS LV RV IVS LV
P
Normalized intensity
0.3
0.2
0.1
0.0
p<0.05
Control
DTA
Relative R/L position
R
Normalized intensity
0.50
0.25
0.00
p<0.05
Relative R/L position

850 **Figure 3. Cell ablation of *Tbx5*$^{+}$/*Mef2cAHF*$^{+}$ progenitors causes RV hypoplasia, IVS**
851 **disorganization, and lineage mixing.** Misexpression of *diphtheria toxin* (*DTA*) in
852 *Tbx5*$^{+}$/*Mef2cAHF*$^{+}$ progenitors in *Tbx5*$^{CreERT2/+}$;*Mef2cAHF-DreERT2*;*ROSA26*$^{Ai66/+}$;*Hip11*$^{intersectional-}$
853 $^{DTA/+}$ embryos (*DTA*), compared to *Tbx5*$^{CreERT2/+}$;*Mef2cAHF-DreERT2*;*ROSA26*$^{Ai66/+}$;*Hip11*$^{+/+}$
854 (control), resulted in RV hypoplasia (arrows) at E9.5 (A, B), and E12.5 (C-J), along with
855 disorganization and non-compaction of the interventricular septum (IVS) (asterisk) (G-J). (K-N) At
856 E10.5, mixing of the *Mef2cAHF*$^{+}$ lineage and *Tbx5*$^{+}$ lineage (white arrow in N shows ectopic *Tbx5*$^{+}$
857 lineage ZsGreen cell in the right heart) was observed by lightsheet microscopy in
858 *Tbx5*$^{CreERT2/+}$;*Mef2cAHF-DreERT2*;*ROSA26*$^{Ai6/Ai66b}$;*Hip11*$^{intersectional-DTA/+}$ embryos (*DTA*) (n=2)
859 compared to *Tbx5*$^{CreERT2/+}$;*Mef2cAHF-DreERT2*;*ROSA26*$^{Ai6/Ai66b}$;*Hip11*$^{+/+}$ embryos (control) (n=2).
860 (O-R) Linear profiles quantified fluorescence intensity above a threshold (dashed line in P,R)
861 across the heart at the right or left (R/L) positions. *Mef2cAHF*$^{+}$ lineage retreated rightward
862 (depiction in O, purple arrow in P) while *Tbx5*$^{+}$ lineage cells expanded rightward into the RV
863 (depiction in Q, green arrow in R), consistent with a compartment boundary disruption. Yellow
864 shading represents *Tbx5*$^{+}$/*Mef2cAHF*$^{+}$ lineage cells and region of cell ablation. Statistical
865 significance ($p<0.05$) between control and *DTA* mutants was determined by Welch's two-sample
866 t-test at each position along the right-left axis.
867
868

Figure S3

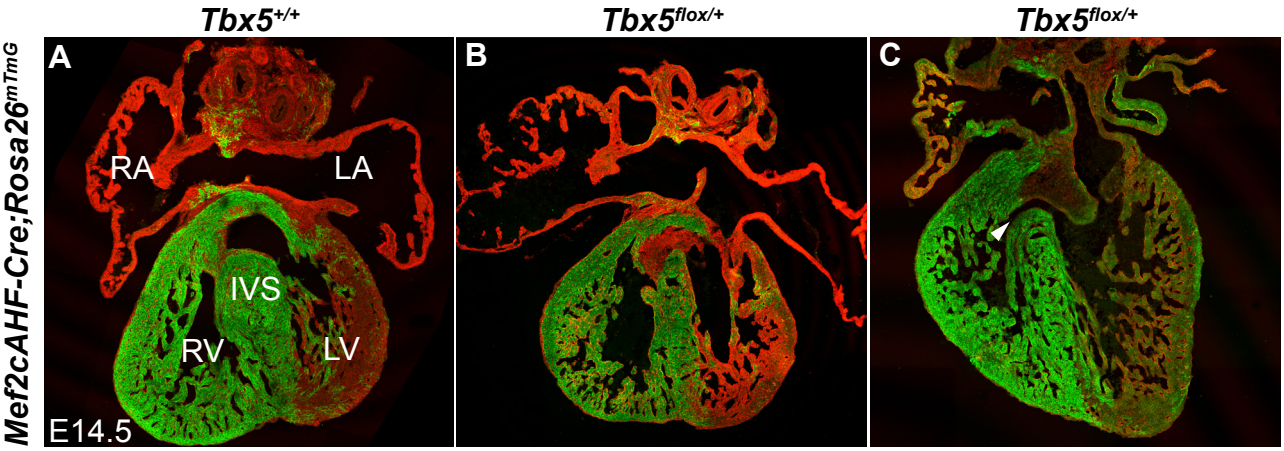
Tbx5+/+
Tbx5flox/+
Tbx5flox/+
Mef2cAHF-Cre;Rosa26mTmG
A
B
C
RA
LA
IVS
RV
LV
E14.5

869 **Supplemental Figure 3. Conditional haploinsufficiency of *Tbx5* in the interventricular**
870 **septum (IVS) leads to ventricular septal defects (VSDs).** (A-C) At E14.5, membranous VSDs
871 were observed in *Mef2cAHF-Cre*;*ROSA26*$^{mTmG/+}$;*Tbx5*$^{flox/+}$ mutant embryos (n=4/7) compared to
872 *Mef2cAHF-Cre*;*ROSA26*$^{mTmG/+}$;*Tbx5*$^{flox/+}$ controls (n=0/3).
873
874

Figure 4

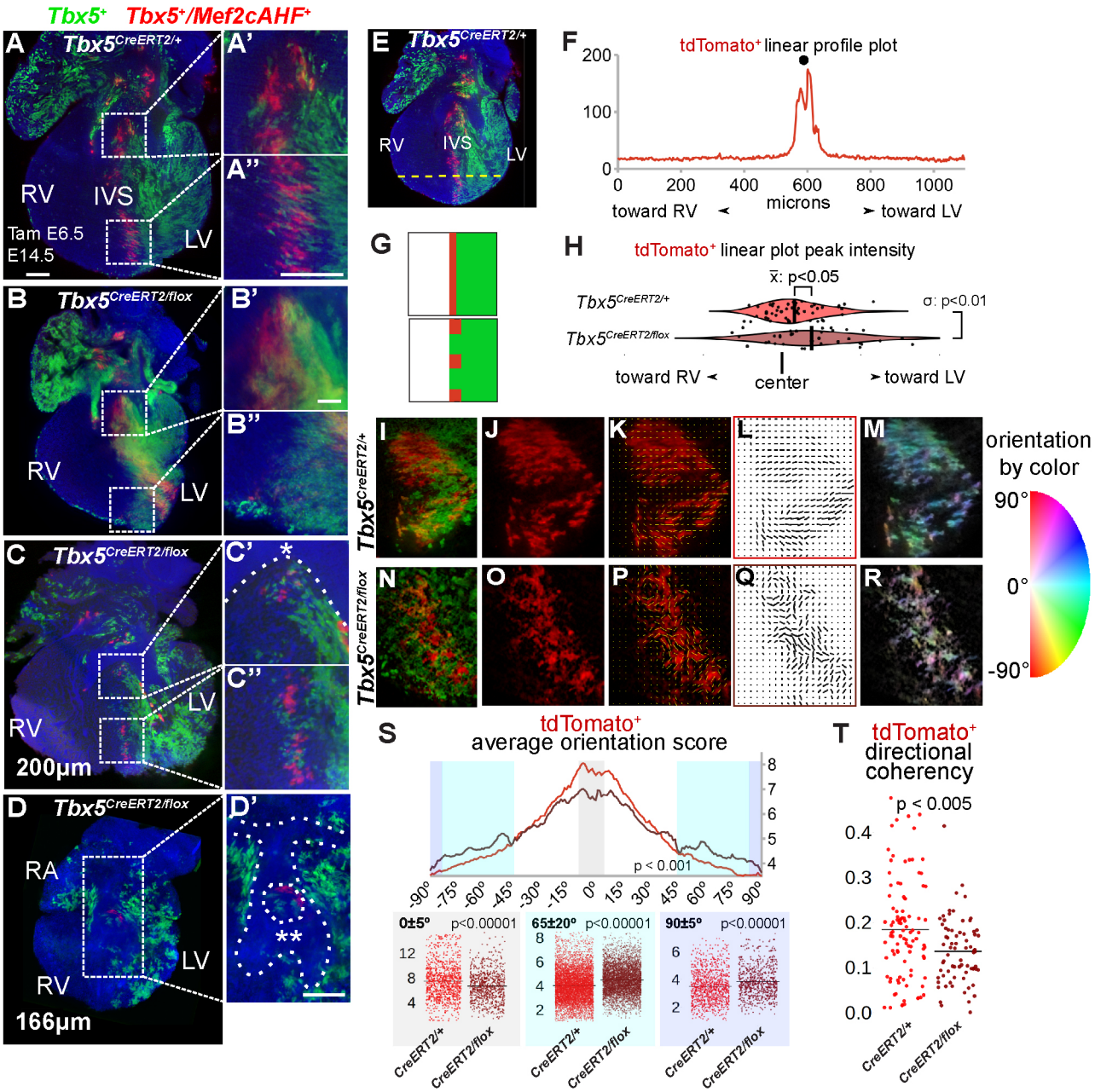
Tbx5+ Tbx5+/Mef2cAHF+
A Tbx5CreERT2/+
A'
A''
RV
IVS
LV
Tam E6.5
E14.5
B Tbx5CreERT2/flox
B'
B''
RV
LV
C Tbx5CreERT2/flox
C'
C''
*
RV
LV
200µm
D Tbx5CreERT2/flox
D'
**
RA
RV
LV
166µm
E Tbx5CreERT2/+
RV
IVS
LV
F
tdTomato+ linear profile plot
200
100
0
0 200 400 600 800 1000
toward RV
microns
toward LV
G
H
tdTomato+ linear plot peak intensity
x̄: p<0.05
σ: p<0.01
Tbx5CreERT2/+
Tbx5CreERT2/flox
toward RV
center
toward LV
I J K L M
N O P Q R
Tbx5CreERT2/+
Tbx5CreERT2/flox
orientation by color
90°
0°
-90°
S
tdTomato+
average orientation score
p < 0.001
-90° -75° -60° -45° -30° -15° 0° 15° 30° 45° 60° 75° 90°
0±5° p<0.00001
65±20° p<0.00001
90±5° p<0.00001
CreERT2/+
CreERT2/flox
T
tdTomato+
directional
coherency
p < 0.005
0.4
0.3
0.2
0.1
0.0
CreERT2/+
CreERT2/flox

875 **Figure 4. Reduced Tbx5 dosage caused ventricular septal defects and perturbations to IVS**
876 **boundary position and integrity.** (A) Mid-posterior optical sections from light sheet microscopy
877 of a control (*Tbx5*$^{CreERT2/+}$;*Mef2cAHF-DreERT2*;*ROSA26*$^{Ai6/Ai66}$) heart display *Tbx5*$^{+}$ lineage
878 (ZsGreen) and *Tbx5*$^{+}$*/Mef2cAHF*$^{+}$ lineage (tdTomato immunostaining) cells. *Tbx5*$^{+}$*/Mef2cAHF*$^{+}$
879 lineage cells in the interventricular septum (IVS) extended from the base (A') to the apex (A") of
880 the heart, where cells were highly organized. (B-D) A spectrum of phenotypes of *Tbx5*$^{CreERT2/flox}$
881 mutants (*Tbx5*$^{CreERT2/flox}$*;Mef2cAHF-DreERT2*;*ROSA26*$^{Ai6/Ai66}$) were observed, including intact IVS
882 (B-B"), membranous VSD (C-C", asterisk) and atrioventricular septal defect (double asterisk in
883 D'). (B', B", C', C", D') A reduction, maldistribution and disorientation of *Tbx5*$^{+}$*/Mef2cAHF*$^{+}$ lineage
884 cells were observed in *Tbx5*$^{CreERT2/flox}$ mutants. (E-H) Linear plot profiles at positions along the
885 anterior-posterior and apical-basal axis of control (n=4) and *Tbx5*$^{CreERT2/flox}$ mutant (n=3) hearts for
886 *Tbx5*$^{+}$*/Mef2cAHF*$^{+}$ lineage cells showed a leftward shift of boundary positioning and broadening
887 of the *Tbx5*$^{+}$*/Mef2cAHF*$^{+}$ lineage position, consistent with lineage mixing. (E,F) An example of a
888 linear profile plot is shown, and (G,H) aggregated data is depicted and quantified. (I-T) Orientation
889 scores for cells from each channel (tdTomato^{+} or ZsGreen^{+}) was delineated for each genotype,
890 and distributions were plotted as a function of angle. *Tbx5*$^{CreERT2/flox}$ mutant hearts scored worse
891 for orientation of *Tbx5*$^{+}$*/Mef2cAHF*$^{+}$ lineage (tdTomato^{+}) cells in the dominant direction (range
892 from -5 to 5 degrees) and scored higher in the orientation orthogonal to the dominant direction
893 (range from 85 to 95 degrees and -85 to -95 degrees), as determined (S) by Watson's two-sample
894 test across all orientations or by Wilcoxon signed-rank test for selected orientations. (T)
895 *Tbx5*$^{+}$*/Mef2cAHF*$^{+}$ lineage (tdTomato^{+}) cells demonstrated worse directional coherency scoring in
896 *Tbx5*$^{CreERT2/flox}$ mutants by Wilcoxon signed-rank test.
897
898

Figure S4

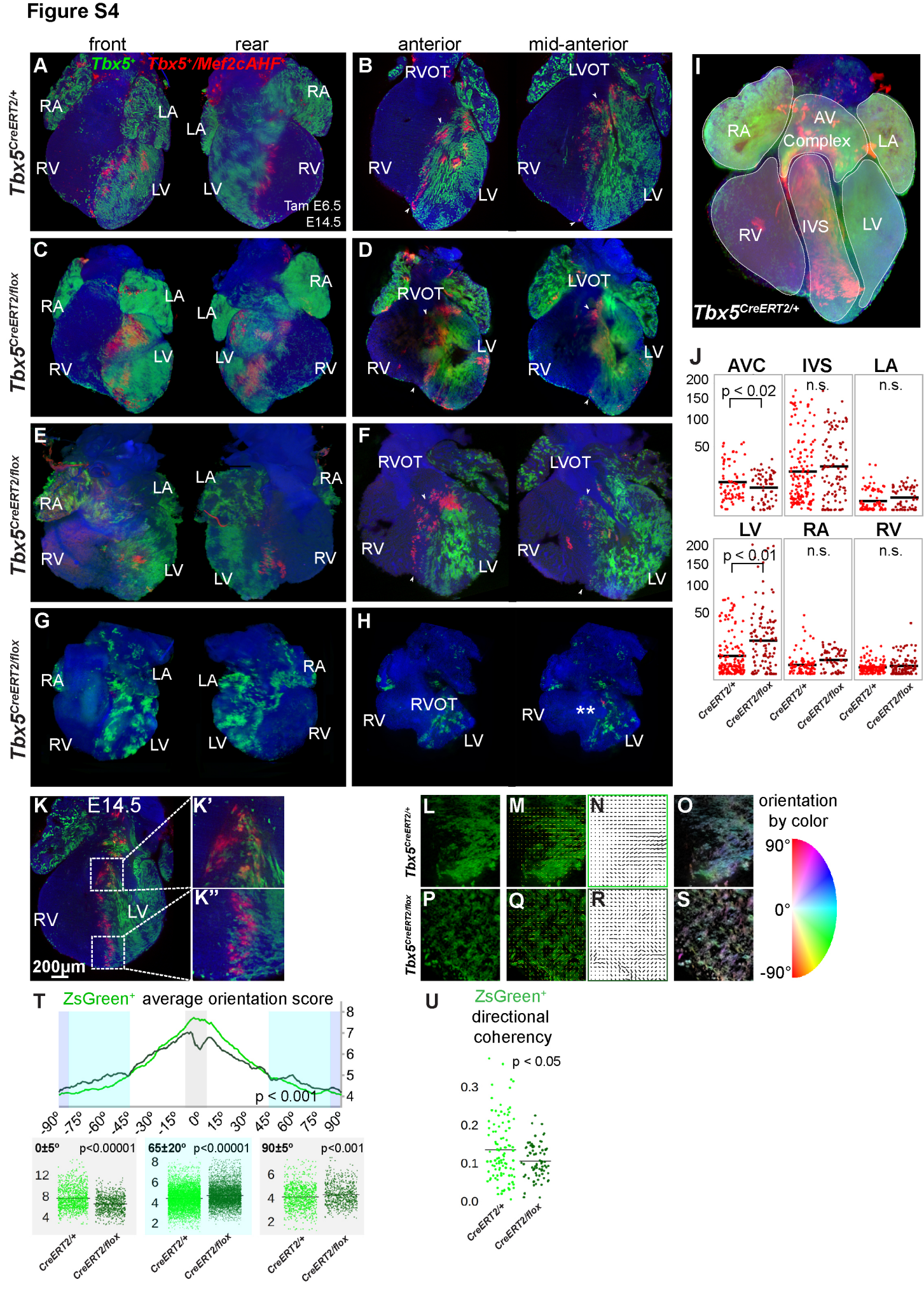
front
rear
anterior
mid-anterior
A
Tbx5+
Tbx5+/Mef2cAHF+
RA
LA
RV
LV
Tam E6.5
E14.5
B
RVOT
LVOT
C
D
E
F
G
H
**
Tbx5CreERT2/+
Tbx5CreERT2/flox
I
AV
Complex
IVS
J
AVC
IVS
LA
LV
RA
RV
p < 0.02
p < 0.01
n.s.
CreERT2/+
CreERT2/flox
K
E14.5
K'
K''
200µm
L
M
N
O
P
Q
R
S
orientation
by color
90°
0°
-90°
T
ZsGreen+ average orientation score
p < 0.001
-90°
-75°
-60°
-45°
-30°
-15°
0°
15°
30°
45°
60°
75°
90°
0±5°
p<0.00001
65±20°
p<0.00001
90±5°
p<0.001
U
ZsGreen+
directional
coherency
p < 0.05

Supplemental Figure 4. (A-H) Volume renderings from lightsheet microscopy of anterior and posterior surfaces, as well as anterior and mid-anterior 4-chamber optical sections of *Tbx5*$^{CreERT2/+}$ control (*Tbx5*$^{CreERT2/+}$;*Mef2cAHF-DreERT2*;*ROSA26*$^{Ai6/Ai66}$) and *Tbx5*$^{CreERT2/flox}$ mutant (*Tbx5*$^{CreERT2/flox}$;*Mef2cAHF-DreERT2*;*ROSA26*$^{Ai6/Ai66}$) hearts at E14.5 display *Tbx5*$^{+}$ lineage (ZsGreen) and *Tbx5*$^{+}$/*Mef2cAHF*$^{+}$ lineage (tdTomato immunostaining) cells. (I, J) Quantification of the anatomical location of tdTomato^{+} and ZsGreen^{+} cells in *Tbx5*$^{CreERT2/flox}$ mutants (n=4) and *Tbx5*$^{CreERT2/+}$ controls (n=4), by region as outlined in (I). Over 1200 3-dimensional regions of interest were drawn blinded, and then integrated fluorescence signal was assessed. (J) Although no regional differences in the intensities of ZsGreen^{+} were detected, tdTomato^{+} displayed higher integrated fluorescence in the left ventricle (LV) and less signal in atrioventricular canal (AVC) by Wilcoxon signed-rank test. (L-U) *Tbx5*$^{CreERT2/flox}$ mutant hearts scored worse for orientation scores of *Tbx5*$^{+}$ lineage (ZsGreen^{+}) cells in the dominant direction (range from -5 to 5 degrees) and scored higher in the orientation orthogonal to the dominant direction (range from 85 to 95 degrees and -85 to -95 degrees), as determined (T) by Watson's two-sample test across all orientations or by Wilcoxon signed-rank test for selected orientations. (U) *Tbx5*$^{+}$ lineage (ZsGreen^{+}) cells demonstrated worse directional coherency scoring in *Tbx5*$^{CreERT2/flox}$ mutants by Wilcoxon signed-rank test.

Video 2. Related to Figure 4 and Supplemental Figure 4.

Figure 5

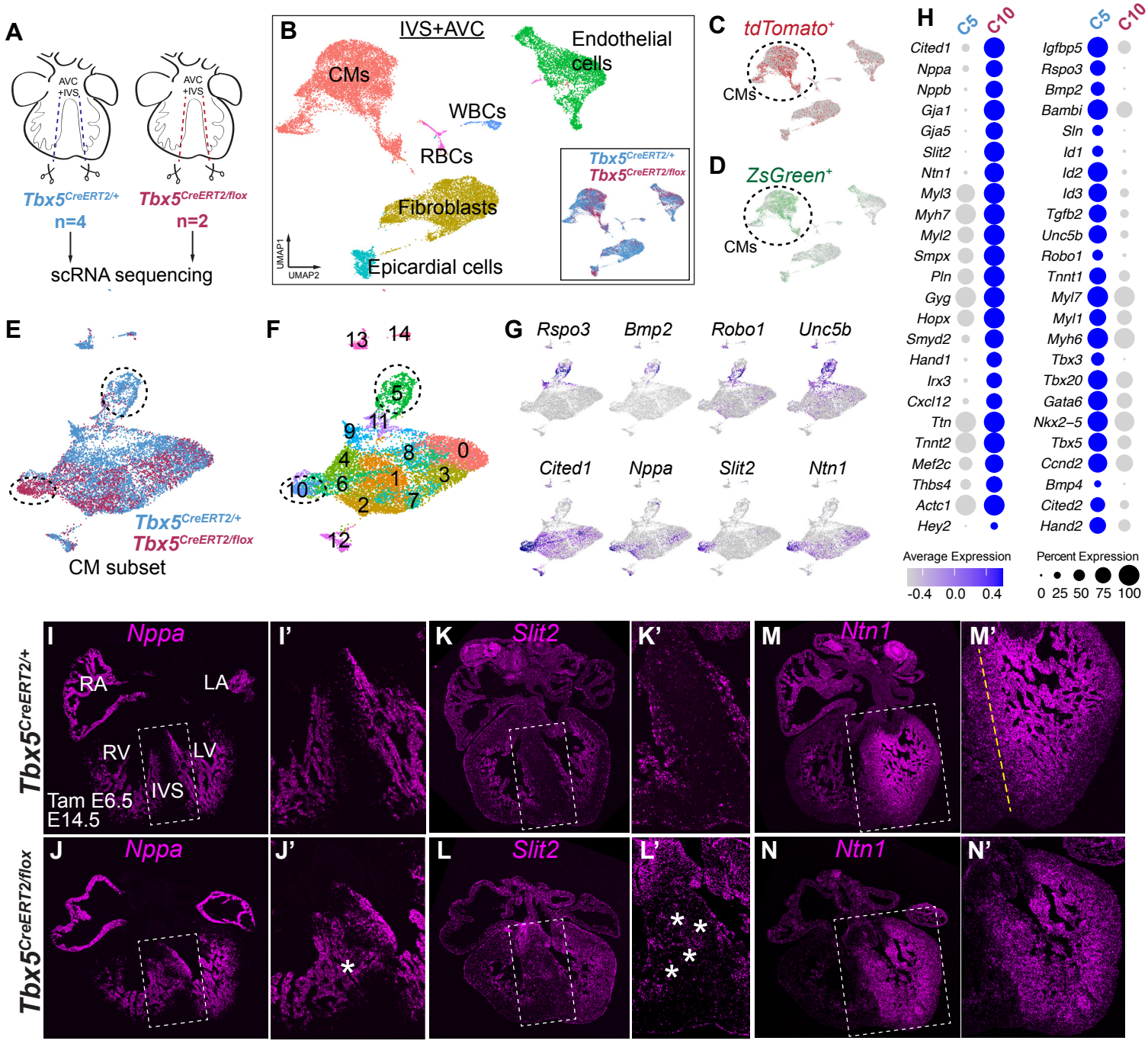
A
AVC
+IVS
Tbx5CreERT2/+
n=4
Tbx5CreERT2/flox
n=2
scRNA sequencing
B
IVS+AVC
CMs
Endothelial cells
WBCs
RBCs
Fibroblasts
Epicardial cells
UMAP1
UMAP2
Tbx5CreERT2/+
Tbx5CreERT2/flox
C
tdTomato+
CMs
D
ZsGreen+
CMs
E
Tbx5CreERT2/+
Tbx5CreERT2/flox
CM subset
F
13
14
5
11
9
8
0
4
1
3
10
6
2
7
12
G
Rspo3
Bmp2
Robo1
Unc5b
Cited1
Nppa
Slit2
Ntn1
H
C5
C10
Cited1
Nppa
Nppb
Gja1
Gja5
Slit2
Ntn1
Myl3
Myh7
Myl2
Smpx
Pln
Gyg
Hopx
Smyd2
Hand1
Irx3
Cxcl12
Ttn
Tnnt2
Mef2c
Thbs4
Actc1
Hey2
Igfbp5
Rspo3
Bmp2
Bambi
Sln
Id1
Id2
Id3
Tgfb2
Unc5b
Robo1
Tnnt1
Myl7
Myl1
Myh6
Tbx3
Tbx20
Gata6
Nkx2–5
Tbx5
Ccnd2
Bmp4
Cited2
Hand2
Average Expression
-0.4 0.0 0.4
Percent Expression
0 25 50 75 100
Tbx5CreERT2/+
Tbx5CreERT2/flox
I
Nppa
RA
LA
RV
LV
IVS
Tam E6.5
E14.5
I'
K
Slit2
K'
M
Ntn1
M'
J
Nppa
J'
L
Slit2
L'
N
Ntn1
N'

Figure 5. *Slit2* and *Ntn1* are *Tbx5*-sensitive genes in the interventricular septum (IVS). (A) At E13.5, we micro-dissected the right ventricle (RV), left ventricle (LV) and IVS+atrioventricular canal (AVC) in *Tbx5*$^{CreERT2/+}$ controls (n=4) and *Tbx5*$^{CreERT/flox}$ mutants (*Tbx5*$^{CreERT2/flox}$*;Mef2cAHF-DreERT2*;*ROSA26*$^{Ai6/Ai66}$)(n=2) with the labeled *Tbx5*$^{+}$*/Mef2cAHF*$^{+}$ lineage (*tdTomato*$^{+}$) and *Tbx5*$^{+}$ lineage (*ZsGreen*$^{+}$) cells, after tamoxifen at E6.5. (B) UMAP visualization by cell type clusters and *Tbx5* genotype (inset). CMs, cardiomyocytes; WBCs, white blood cells; RBCs, red blood cells. (C) *ZsGreen*$^{+}$ and (D) *tdTomato*$^{+}$ cells are enriched among CMs. (E) UMAP shows a *Tnnt2*$^{+}$ CM subset by *Tbx5* genotype or (F) Louvain clusters. (G) Feature plots show that atrioventricular canal genes (*Rspo3, Bmp2, Robo1, Unc5b*) are enriched among control-enriched cluster 5, suggesting downregulation of these genes in *Tbx5* mutants. Trabecular genes (*Cited1, Nppa, Slit2, Ntn1*) were enriched in the *Tbx5* mutant-enriched cluster 10. (H) Dot plots of selected genes that are upregulated in cluster 10 (C10) or in cluster 5 (C5). Significance of adj $p<0.05$ was determined by Wilcoxan rank sum. (I-N) Fluorescent *in situ* hybridization of trabecular genes *Nppa*, *Slit2* and *Ntn1* in *Tbx5*$^{CreERT2/+}$ controls or *Tbx5*$^{CreERT2/flox}$ mutants at E14.5. (I, I', K, K') *Nppa* and *Slit2* are normally expressed in the ventricular trabecular layer and excluded from the core of the IVS. (J, J', L, L') In a *Tbx5*$^{CreERT2/flox}$ mutant with an intact IVS, *Nppa* and *Slit2* are misexpressed in the IVS (asterisks). (M, M') *Ntn1* is normally expressed in the trabecular layer and in a gradient across the IVS from left to right, demarcated by yellow dashed line. (N, N') In a *Tbx5*$^{CreERT2/flox}$ mutant with an intact IVS, *Ntn1* is expanded across the IVS, flattening its gradient.

Figure S5

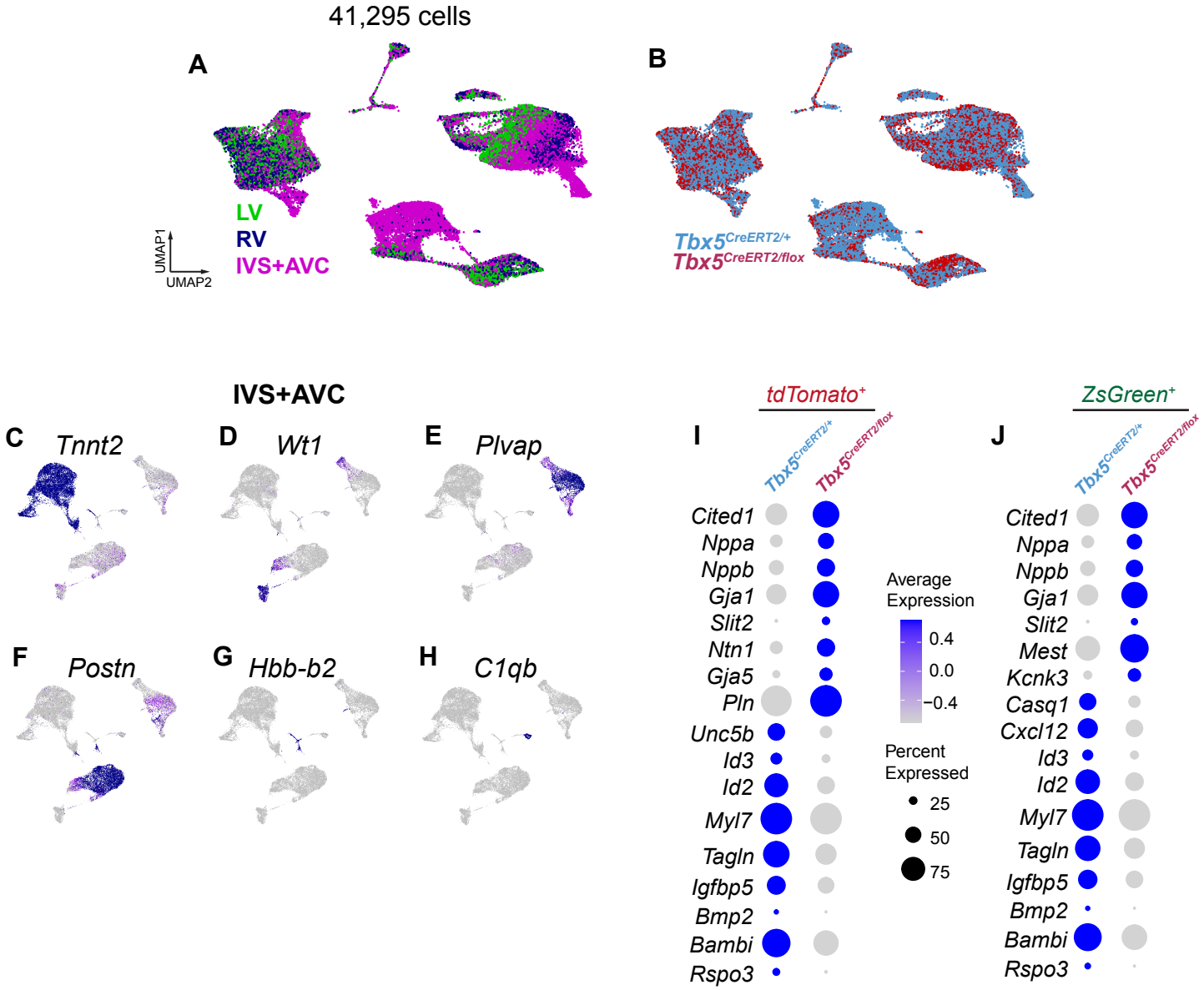
41,295 cells
A
LV
RV
IVS+AVC
UMAP1
UMAP2
B
Tbx5CreERT2/+
Tbx5CreERT2/flox
IVS+AVC
C Tnnt2
D Wt1
E Plvap
F Postn
G Hbb-b2
H C1qb
I
tdTomato+
Tbx5CreERT2/+
Tbx5CreERT2/flox
Cited1
Nppa
Nppb
Gja1
Slit2
Ntn1
Gja5
Pln
Unc5b
Id3
Id2
Myl7
Tagln
Igfbp5
Bmp2
Bambi
Rspo3
Average Expression
0.4
0.0
−0.4
Percent Expressed
25
50
75
J
ZsGreen+
Tbx5CreERT2/+
Tbx5CreERT2/flox
Cited1
Nppa
Nppb
Gja1
Slit2
Mest
Kcnk3
Casq1
Cxcl12
Id3
Id2
Myl7
Tagln
Igfbp5
Bmp2
Bambi
Rspo3

Supplemental Figure 5. In scRNA-seq samples from E13.5 hearts (control, n=4; *Tbx5* mutant, n=3), we display cells by region (LV, RV, IVS) (A) or by genotype (B). IVS+AVC region (control, n=4, *Tbx5* mutant, n=2), we detected clusters enriched for (C) *Tnnt2*$^+$ cardiomyocytes (CMs), (D) *Tbx18*$^+$/*Wt1*$^+$ epicardial cells, (E) *Plvap*$^+$ endothelial cells, (F) *Postn*$^+$ fibroblasts, (G) *Hbb-b2*$^+$ red blood cells, and (H) *C1qb*$^+$ white blood cells. Dot plots of selected differentially expressed genes in (I) *tdTomato*$^+$ or (J) *ZsGreen*$^+$ cells from the IVS+AVC region. Significance of adj $p<0.05$ was determined by Wilcoxan rank sum.

Figure S6

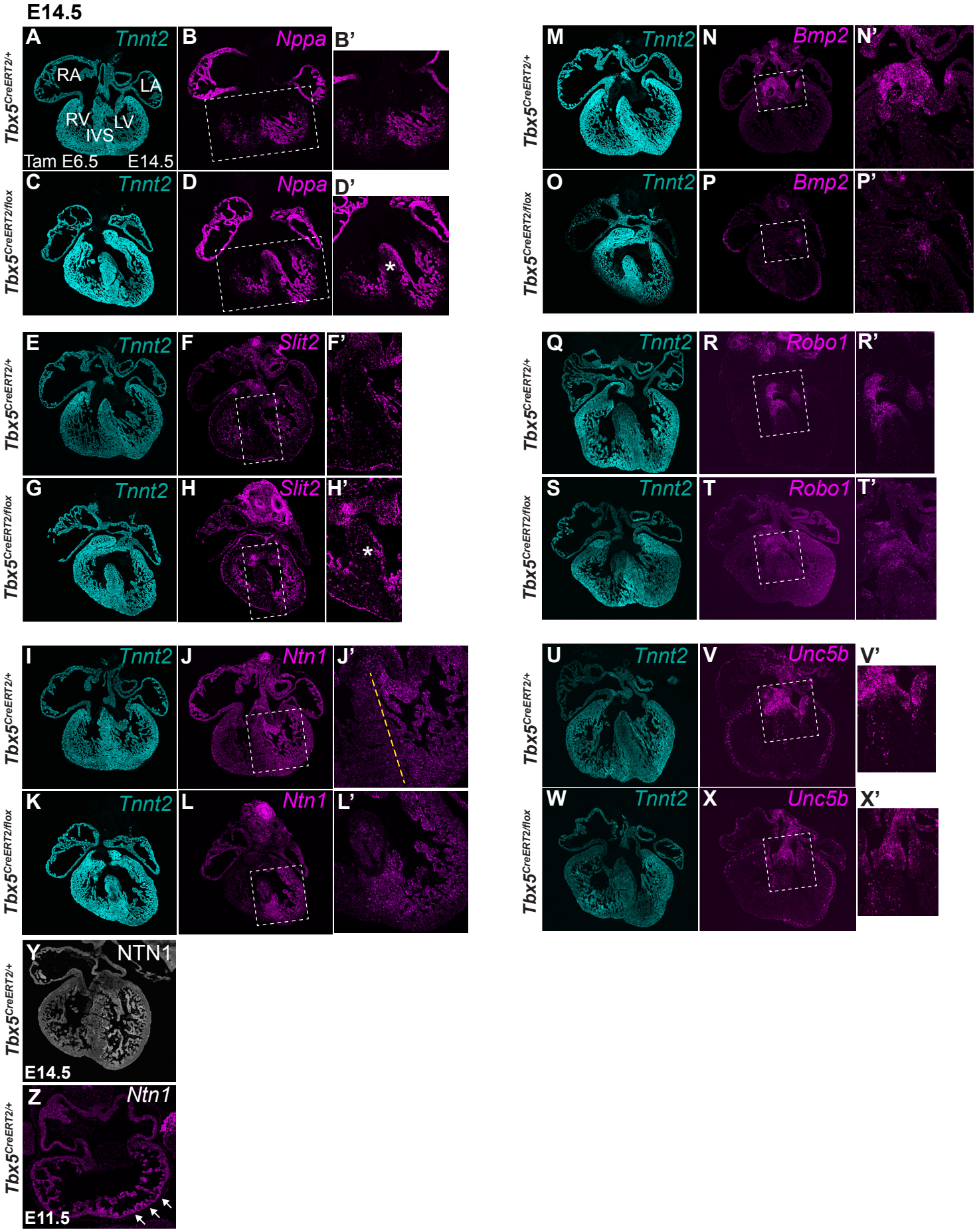
E14.5
A
Tnnt2
RA
LA
RV
LV
IVS
Tam E6.5
E14.5
B
Nppa
B'
C
Tnnt2
D
Nppa
D'
*
M
Tnnt2
N
Bmp2
N'
O
Tnnt2
P
Bmp2
P'
E
Tnnt2
F
Slit2
F'
G
Tnnt2
H
Slit2
H'
*
Q
Tnnt2
R
Robo1
R'
S
Tnnt2
T
Robo1
T'
I
Tnnt2
J
Ntn1
J'
K
Tnnt2
L
Ntn1
L'
U
Tnnt2
V
Unc5b
V'
W
Tnnt2
X
Unc5b
X'
Y
NTN1
E14.5
Z
Ntn1
E11.5
Tbx5CreERT2/+
Tbx5CreERT2/flox

Supplemental Figure 6. Fluorescent *in situ* hybridization of *Tbx5*-dependent genes. (A-L') Fluorescent *in situ* hybridization at E14.5 after tamoxifen at E6.5 of *Nppa*, *Slit2* and *Ntn1* are expressed in the trabecular layer in *Tbx5*$^{CreERT2/+}$ controls (*Tbx5*$^{CreERT2/+}$;*Mef2cAHF-DreERT2*;*ROSA26*$^{Ai6/Ai66}$), and misexpressed in the IVS in *Tbx5*$^{CreERT2/flox}$ mutants (*Tbx5*$^{CreERT2/flox}$;*Mef2cAHF-DreERT2*;*ROSA26*$^{Ai6/Ai66}$) with a membranous VSD at E14.5. Yellow dashed line demarcates gradient of *Ntn1* expression across the IVS from left to right. *Tnnt2* is expressed in cardiomyocytes. (M-X') Expression of *Bmp2*, *Robo1* and *Unc5b* are expressed in the atrioventricular canal (boxed region) in *Tbx5*$^{CreERT2/+}$ controls, and expression of these genes are reduced in *Tbx5*$^{CreERT2/flox}$ mutants. (Y) Immunostaining of NTN1 at E14.5. (Z) Fluorescent *in situ* hybridization of *Ntn1* at E11.5. Asterisks indicate ectopic expression. Arrows highlight enriched expression.

Figure S7

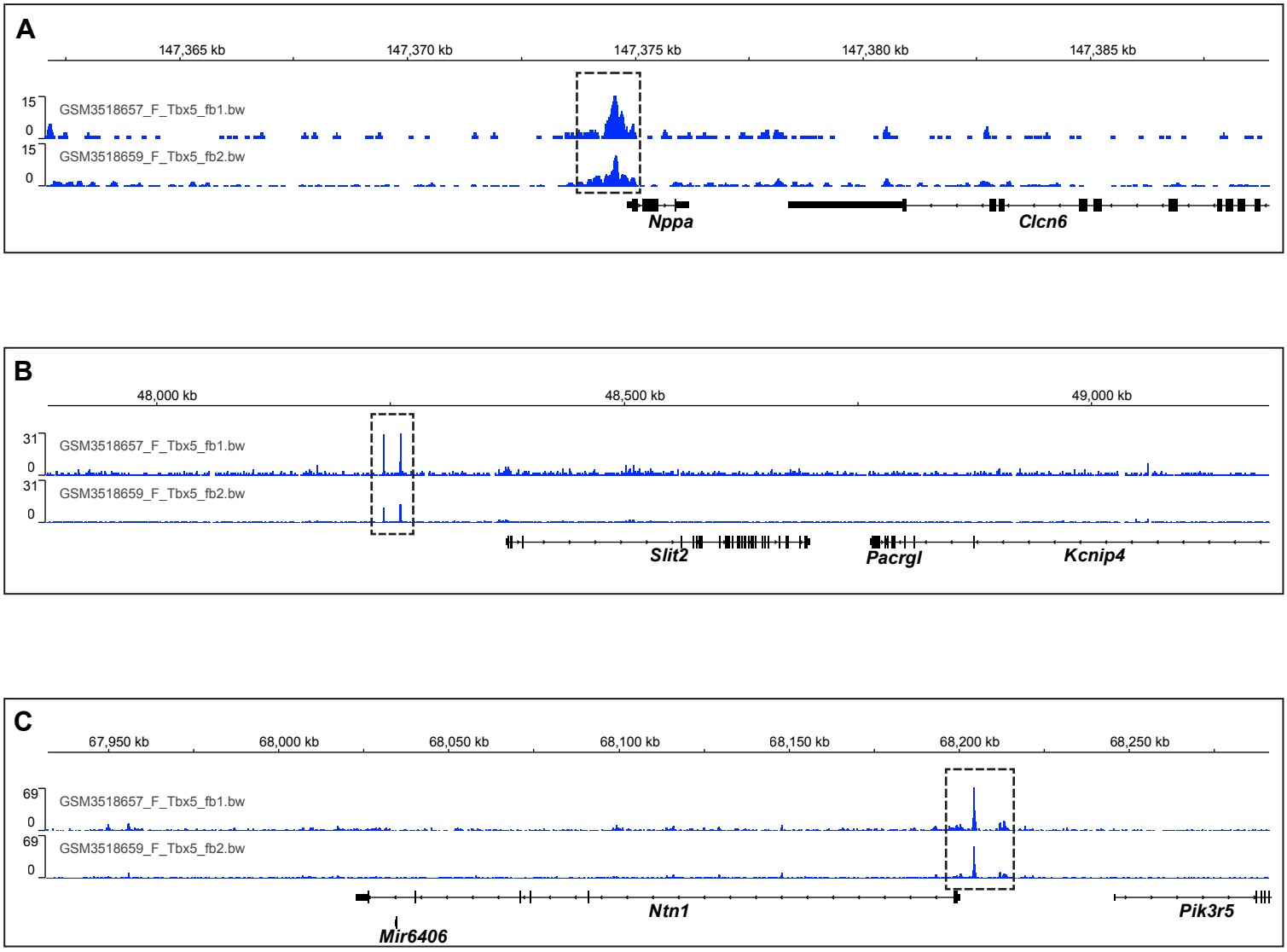
A
147,365 kb
147,370 kb
147,375 kb
147,380 kb
147,385 kb
15
0
GSM3518657_F_Tbx5_fb1.bw
15
0
GSM3518659_F_Tbx5_fb2.bw
Nppa
Clcn6
B
48,000 kb
48,500 kb
49,000 kb
31
0
GSM3518657_F_Tbx5_fb1.bw
31
0
GSM3518659_F_Tbx5_fb2.bw
Slit2
Pacrgl
Kcnip4
C
67,950 kb
68,000 kb
68,050 kb
68,100 kb
68,150 kb
68,200 kb
68,250 kb
69
0
GSM3518657_F_Tbx5_fb1.bw
69
0
GSM3518659_F_Tbx5_fb2.bw
Mir6406
Ntn1
Pik3r5

963 **Supplemental Figure 7. TBX5 chromatin occupancy near *Slit2* and *Ntn1*.** (A-C) Browser
964 tracks of TBX5 ChIP-seq from E12.5 hearts [32] shows peaks of TBX5 occupancy (boxed in red)
965 near promoters of *Nppa*, *Slit2* and *Ntn1*.
966
967

Figure S8

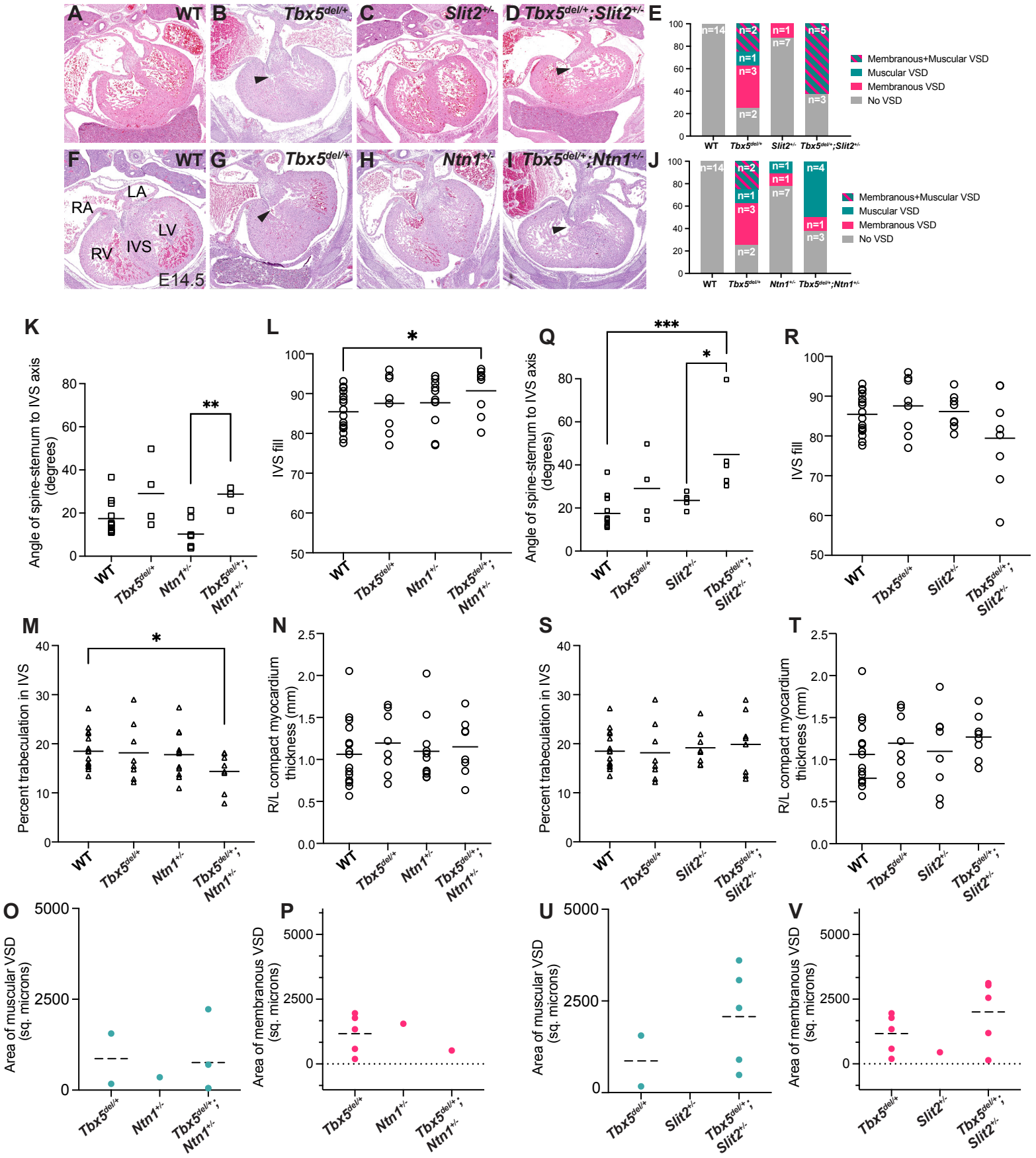
A WT
B Tbx5del/+
C Slit2+/-
D Tbx5del/+;Slit2+/-
E
F WT
G Tbx5del/+
H Ntn1+/-
I Tbx5del/+;Ntn1+/-
J
RA
LA
LV
RV
IVS
E14.5
Membranous+Muscular VSD
Muscular VSD
Membranous VSD
No VSD
K
L
Q
R
M
N
S
T
O
P
U
V
Angle of spine-sternum to IVS axis (degrees)
IVS fill
Percent trabeculation in IVS
R/L compact myocardium thickness (mm)
Area of muscular VSD (sq. microns)
Area of membranous VSD (sq. microns)
WT
Tbx5del/+
Ntn1+/-
Tbx5del/+; Ntn1+/-
Slit2+/-
Tbx5del/+; Slit2+/-

968 **Supplemental Figure 8. *Tbx5-Ntn1* and *Tbx5-Slit2* genetic interactions.** Histology from E14.5
969 embryos from matings of (A-D) *Tbx5*$^{del/+}$ and *Slit2*$^{+/-}$ or (F-I) *Tbx5*$^{del/+}$ and *Ntn1*$^{+/-}$ by genotype.
970 Arrowheads depict muscular ventricular septal defects (VSDs). (E,J) Quantification of
971 membranous or muscular VSDs by genotype. *Tbx5*$^{del/+}$;*Slit2*$^{+/-}$compound heterozygous embryos
972 displayed an estimated decrease in the incidence of membranous VSDs, which approached
973 significance (log OR -2.5; $p<0.09$ in a Generalized Linear Model). *Tbx5*$^{del/+}$;*Ntn1*$^{+/-}$ compound
974 heterozygous embryos displayed a decrease of membranous VSDs (log OR -5.3; $p<1x10^{-3}$ by a
975 Generalized Linear Model), but not changes to prevalence of muscular VSDs (log OR 0.12;
976 $p<0.93$). Machine-learning based quantitative morphometry of metrics for (K-P) *Tbx5*$^{del/+}$ and
977 *Ntn1*$^{+/-}$ or (Q-V) *Tbx5*$^{del/+}$ and *Slit2*$^{+/-}$ by genotype. IVS, interventricular septum. Significance
978 determined by Fisher's exact test (*$p<0.05$, **$p<0.01$, ***$p<0.001$).
979
980

Figure 6

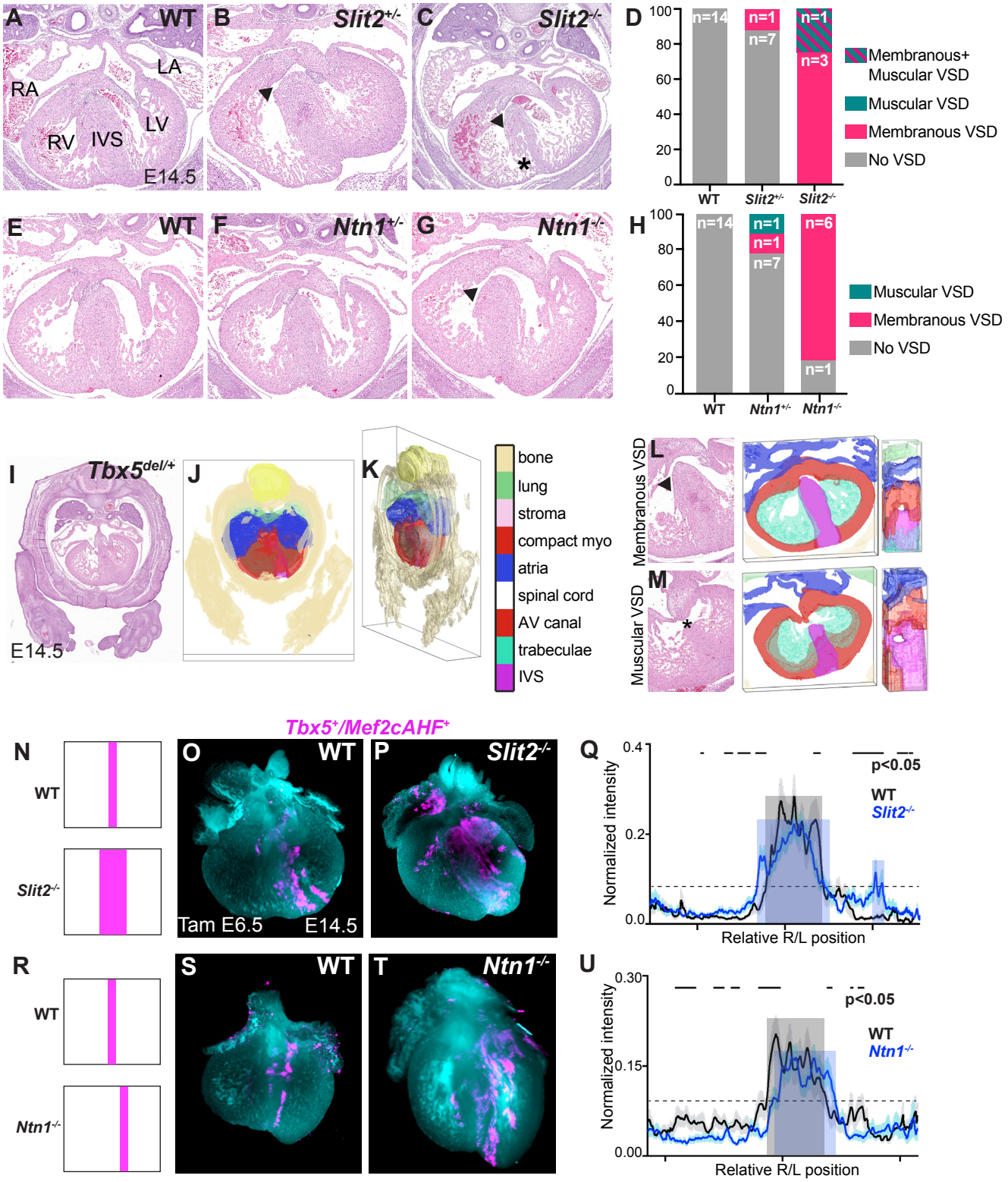
A
WT
RA
LA
RV
IVS
LV
E14.5
B
Slit2+/-
C
Slit2-/-
D
n=14
n=1
n=7
n=1
n=3
Membranous+ Muscular VSD
Muscular VSD
Membranous VSD
No VSD
WT
Slit2+/-
Slit2-/-
E
WT
F
Ntn1+/-
G
Ntn1-/-
H
n=14
n=1
n=1
n=7
n=6
n=1
Muscular VSD
Membranous VSD
No VSD
WT
Ntn1+/-
Ntn1-/-
I
Tbx5del/+
E14.5
J
K
bone
lung
stroma
compact myo
atria
spinal cord
AV canal
trabeculae
IVS
L
Membranous VSD
M
Muscular VSD
Tbx5+/Mef2cAHF+
N
WT
Slit2-/-
O
WT
Tam E6.5
E14.5
P
Slit2-/-
Q
p<0.05
WT
Slit2-/-
Normalized intensity
Relative R/L position
R
WT
Ntn1-/-
S
WT
T
Ntn1-/-
U
p<0.05
WT
Ntn1-/-
Normalized intensity
Relative R/L position

Figure 6. *Slit2* and *Ntn1* are essential for proper ventricular septation and compartment boundary regulation. (A-C) Histology and (D) incidence of muscular or membranous (arrowhead) ventricular septal defects (VSDs) of *Slit2* mutants are shown. Asterisk demarcates non-compacted interventricular septum (IVS) (E-G) Histology and (H) incidence of muscular or membranous ventricular septal defects (VSDs) of *Ntn1* mutants are shown. (I-K) Machine learning-based 3-D reconstructions of the embryonic heart and other tissues from histology at E14.5 were used for quantitative morphometric analysis of the embryonic heart (Supplemental Figure 7, Supplemental Figure 8). Compact myo, compact myocardium; AV canal, atrioventricular canal; IVS, interventricular septum. (L,M) A 3-D reconstruction of a membranous ventricular septal defect (VSD) anteriorly and muscular VSD posteriorly from a *Tbx5*$^{del/+}$ mutant heart. (N-P) Lightsheet imaging of *Slit2*$^{-/-}$ mutant (*Tbx5*$^{CreERT2/+}$;*Mef2cAHF-DreERT2*;*ROSA26*$^{Ai66/+}$;*Slit2*$^{-/-}$)(n=4) hearts at E14.5 showed a broadened distribution of the *Tbx5*$^{+}$/*Mef2cAHF*$^{+}$ lineage (tdTomato^{+} immunostaining) compared to controls (*Tbx5*$^{CreERT2/+}$;*Mef2cAHF-DreERT2*;*ROSA26*$^{Ai66/+}$;*Slit2*$^{+/+}$)(n=2), as (Q) quantified by linear profiles of fluorescence signals above a threshold (dashed line). Gray shading represents control signal above threshold, and periwinkle represents mutant signal. Significance of $p<0.05$ was determined by Welch's two-sample t-test at each position along the right-left axis. (R-T) Lightsheet imaging of *Ntn1*$^{-/-}$ mutant (*Tbx5*$^{CreERT2/+}$;*Mef2cAHF-DreERT2*;*ROSA26*$^{Ai66/+}$;*Ntn1*$^{-/-}$)(n=6) hearts at E14.5 showed a leftward shift in positioning of the *Tbx5*$^{+}$/*Mef2cAHF*$^{+}$ lineage compared to controls (*Tbx5*$^{CreERT2/+}$;*Mef2cAHF-DreERT2*;*ROSA26*$^{Ai66/+}$;*Ntn1*$^{+/+}$)(n=4), as (U) quantified by linear profiles.

Figure S9

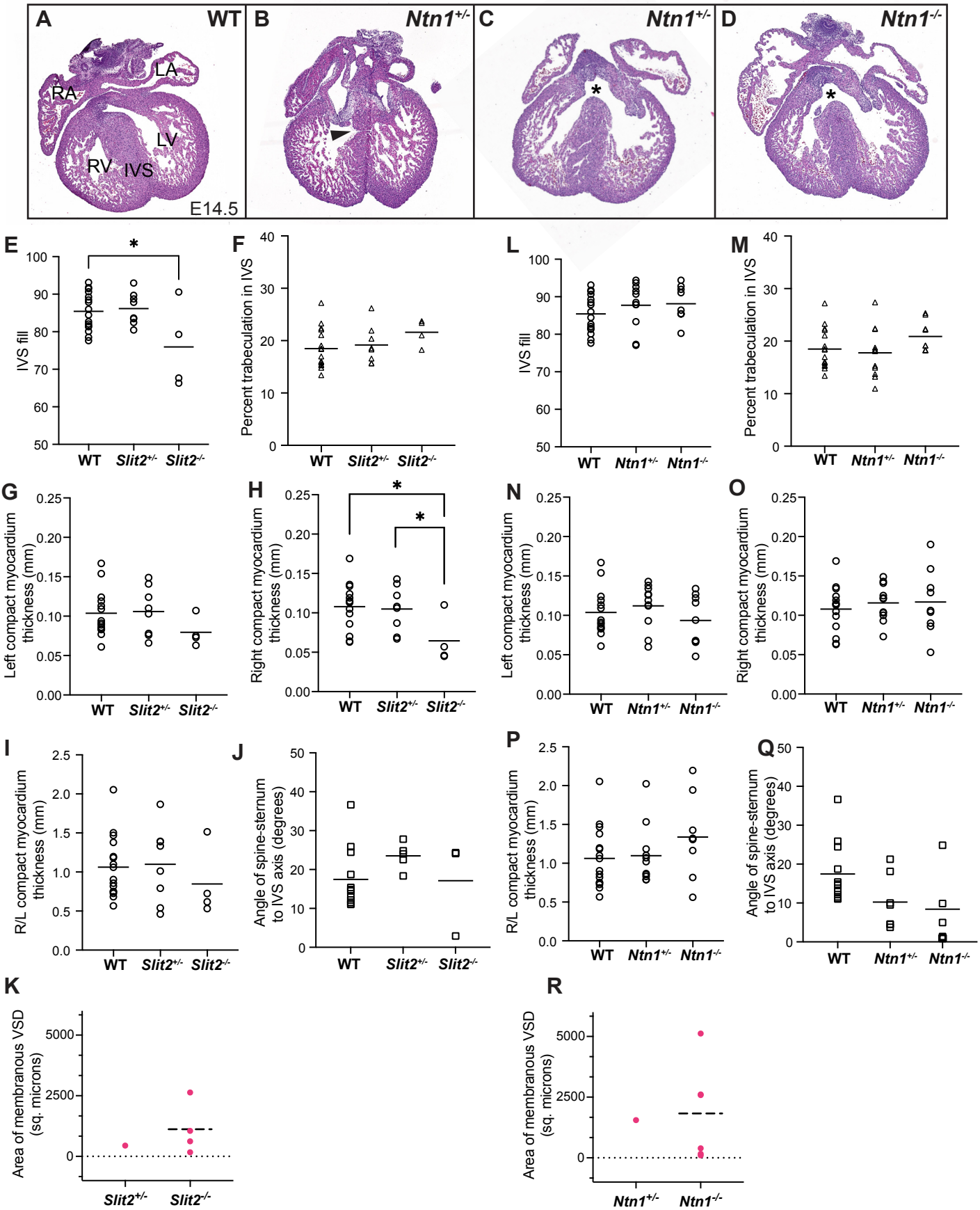
A
WT
RA
LA
LV
RV
IVS
E14.5
B
Ntn1+/-
C
Ntn1+/-
D
Ntn1-/-
E
IVS fill
WT
Slit2+/-
Slit2-/-
F
Percent trabeculation in IVS
L
Ntn1+/-
Ntn1-/-
M
G
Left compact myocardium thickness (mm)
H
Right compact myocardium thickness (mm)
N
O
I
R/L compact myocardium thickness (mm)
J
Angle of spine-sternum to IVS axis (degrees)
P
Q
K
Area of membranous VSD (sq. microns)
R

1004 **Supplemental Figure 9. Quantitative morphometry of *Slit2* and *Ntn1* mutant hearts.** (A-D)
1005 Additional histology by *Ntn1* genotype. Arrowhead, muscular ventricular septal defect (VSD).
1006 Asterisk, membranous VSD. (E-P) Machine learning-based quantitative cardiac morphometrics
1007 for (E-K) *Slit2* or (L-R) *Ntn1* mutants. Significance determined by Fisher's exact test (*$p<0.05$).
1008 (Q,R) Morphometry of the area of membranous VSDs by *Slit2* or *Ntn1* genotypes.